



12-2011

Particle Shielding for Human Spaceflight: Electrostatic Potential Effects on the Störmer Magnetic Dipole Exclusion Region

Benjamin Alan Klamm
bklamm@utk.edu

Recommended Citation

Klamm, Benjamin Alan, "Particle Shielding for Human Spaceflight: Electrostatic Potential Effects on the Störmer Magnetic Dipole Exclusion Region." Master's Thesis, University of Tennessee, 2011.
https://trace.tennessee.edu/utk_gradthes/1076

This Thesis is brought to you for free and open access by the Graduate School at Trace: Tennessee Research and Creative Exchange. It has been accepted for inclusion in Masters Theses by an authorized administrator of Trace: Tennessee Research and Creative Exchange. For more information, please contact trace@utk.edu.

To the Graduate Council:

I am submitting herewith a thesis written by Benjamin Alan Klammer entitled "Particle Shielding for Human Spaceflight: Electrostatic Potential Effects on the Störmer Magnetic Dipole Exclusion Region." I have examined the final electronic copy of this thesis for form and content and recommend that it be accepted in partial fulfillment of the requirements for the degree of Master of Science, with a major in Aerospace Engineering.

Gary A. Flandro, Major Professor

We have read this thesis and recommend its acceptance:

Trevor M. Moeller, Christian G. Parigger

Accepted for the Council:

Carolyn R. Hodges

Vice Provost and Dean of the Graduate School

(Original signatures are on file with official student records.)

**Particle Shielding for Human Spaceflight:
Electrostatic Potential Effects on the Störmer
Magnetic Dipole Exclusion Region**

A Thesis Presented for
the Master of Science Degree
The University of Tennessee, Knoxville

Benjamin Alan Klamm
December 2011

Copyright © 2010 by Benjamin Klamm
All rights reserved.

ACKNOWLEDGEMENTS

My thanks go first and foremost to my wife, Kristina; without her love and support this achievement would have taken years from my life but instead added much more. To Dr. Flandro, I give my sincerest thanks for his honest advice and enabling of my academic career. His unconditional support of this work has been liberating throughout the entire process. I express deep gratitude for Dr. Moeller; his willingness to share his vast knowledge of plasma physics and excellent commentary enabled this work. To Dr. Parigger; his guidance and support in this document and my academic career came ably and without demands for which I wholly appreciate. I would like to especially thank Joshua Batterson for use of his personal computers and excellent counsel, without which my results could not have been completed. To Drs. Jacob and Saad, I give thanks for keeping me well informed and ever-grounded throughout the Master's process. Finally, I am grateful to the countless other students at the University of Tennessee Space Institute, for making my experience a memorable one.

ABSTRACT

A basic hybrid radiation shield concept, consisting of both a monopole positive electrostatic potential barrier and a current-carrying superconducting solenoid, was predicted to provide a more effective method of shielding a habitable torus region than a solenoid acting alone. A randomized position and velocity vector simulation of equal-energy iron ions using a Lagrangian reference frame was performed on the exact magnetic field integral for the solenoid and a discrete summation electrostatic field for a toroidal monopole array approximating a potential surface. Each particle is injected at a specific energy (100, 150 MeV and 1 GeV). Two cases were evaluated at each particle energy modeling 2×10^4 particles. The first case studied effects from only the magnetic dipole field (1.1×10^{13} A m²); the second case evaluated phenomena from a combined magnetic dipole field and electrostatic potential (20 MV). The toroidal electrostatic potential's influence on the size and shape of the Störmer magnetic dipole exclusion region was examined as the main evaluating criterion against the pure magnetic field results. It was shown that the electrostatic potential influences the size of the Störmer dipole exclusion region, and the ratio of particle energy to electrostatic potential is significant in determining the amount increased. It was found that a low particle energy to electrostatic potential ratio of 5:1 increases Störmer area approximately by a factor of 2.

TABLE OF CONTENTS

Chapter	Page
CHAPTER I.....	1
Introduction and General Information	1
1.1 Motivation.....	1
1.2 A General Overview of Radiation Shielding for Human Spaceflight.....	3
CHAPTER II.....	29
Literature Review	29
2.1 Electromagnetic Shielding Research Review	29
CHAPTER III	33
Method of ANALYSIS.....	33
3.1 Numerical Technique	33
3.2 Störmer Region Size Analysis	39
CHAPTER IV	42
Results and Discussion	42
4.1 Code Validation.....	42
4.2 Results	48
CHAPTER V	56
Conclusion	56
LIST OF REFERENCES.....	57
APPENDIX.....	61
Vita	68

LIST OF TABLES

Table	Page
Table 1: Proposed dose equivalent limits (in Sievert) for a mission to Mars [6].	17
Table 2: Results of Störmer area analysis from r-z plots	52
Table 3: Average solar wind properties at 1 AU [5].	62
Table 4: Heliospheric parameters at 1 AU [5].	62

LIST OF FIGURES

Figure	Page
Figure 1: A cutaway view along the x-axis of the conceptual shield design.	2
Figure 2: The full isometric view of the conceptual shield design.....	2
Figure 3: Circular trajectories of charged particles in a uniform and constant magnetic field, directed out of the page [5].	6
Figure 4: Helical trajectory of a negatively charged particle in a uniform and constant magnetic field along the z-axis [5].	6
Figure 5: Magnetic field lines of a dipole [5].	6
Figure 6: Plots of point of closest approach (grey dots) to the origin of 1 GeV Fe^+ trajectories in a magnetic dipole moment of $1.1 \times 10^{13} \text{ A m}^2$ for the entire 360 degree azimuth [3].	8
Figure 7: The motion of a trapped charged particle in Earth's magnetic field [5]. .	9
Figure 8: Location of proton and electron flux densities for the Van Allen radiation belts [26].	9
Figure 9: Schematic diagram of the heliosphere as seen from above the ecliptic north pole [5].	11
Figure 10: Monthly averages of the approx. 1 GeV galactic cosmic ray intensity observed by the Mt. Washington neutron monitor from 1954 through 1979. From Ref. [5], original plot by Ref. [24].	13
Figure 11: Plot of the particle energy flux density spectrum for the typical interplanetary medium [23].	13
Figure 12: Pickup proton velocity as measured by the Ulysses spacecraft. From Ref. [5], original plot from Ref. [25]	15
Figure 13: Several locations with corresponding average dosage per year for humans, in Rems [1].	17

Figure 14: Electrostatic shield concept for lunar base [2].....	20
Figure 15: Electric field strength along z-axis for Figure 14 [2].	20
Figure 16: Three basic configurations for magnetic shielding [27].	23
Figure 17: Basic unbound dipole conceptual design [1].....	24
Figure 18: Bound magnetic shield without y-axis “end plugs” (left) and corresponding magnetic field strength surface, shown for 2 Tesla (right) [28].	26
Figure 19: Comparison between pure electrostatic potential (middle) and a hybrid system (bottom) representing particle collisions with the central potential surface and habitat volume [11].....	31
Figure 20: z-x plot of the electric potential surface as discretized into point charges and generated in three rings.	36
Figure 21: 3D plot of the electric potential surface as discretized into point charges and generated in three rings.	36
Figure 22: Example showing the selection of points for determining the area of the Störmer region using the data brushing tool in MATLAB R2009b.....	40
Figure 23: Example showing the creation of the Delaunay triangulation function in MATLAB R2009b.....	41
Figure 24: Simple test case for 4 th order Runge-Kutta numerical particle mover. Electric and magnetic fields point along the positive z-axis.	43
Figure 25: 3D plot of 1 GeV iron ion trajectories within a magnetic dipole of moment $1.1 \times 10^{13} \text{ A m}^2$	44
Figure 26: Additional 3D plot of 1 GeV iron ion trajectories within a magnetic dipole of moment $1.1 \times 10^{13} \text{ A m}^2$ and a 20 MV positive electrostatic potential.	45
Figure 28: 50,000 iron ions (red dot) simulated at 1 GeV with a solenoid (blue circle) magnetic moment of $1.1 \times 10^{13} \text{ A m}^2$	46
Figure 27: Results from [3] with grey dots representing particles with the solenoid as a red crossed circle.....	46

Figure 29: 20,000 iron ions (red dot) simulated at 1 GeV with a solenoid (blue circle) magnetic moment of $1.1 \times 10^{13} \text{ A m}^2$	49
Figure 30: 20,000 iron ions (red dot) simulated at 1 GeV with a solenoid (blue circle) magnetic moment of $1.1 \times 10^{13} \text{ A m}^2$ and a 20 MV electric potential...	49
Figure 31: 20,000 iron ions (red dot) simulated at 150 MeV with a solenoid (blue circle) magnetic moment of $1.1 \times 10^{13} \text{ A m}^2$	50
Figure 32: 20,000 iron ions (red dot) simulated at 150 MeV with a solenoid (blue circle) magnetic moment of $1.1 \times 10^{13} \text{ A m}^2$ and a 20 MV electric potential. ..	50
Figure 33: 20,000 iron ions (red dot) simulated at 100 MeV with a solenoid (blue circle) magnetic moment of $1.1 \times 10^{13} \text{ A m}^2$	51
Figure 34: 20,000 iron ions (red dot) simulated at 100 MeV with a solenoid (blue circle) magnetic moment of $1.1 \times 10^{13} \text{ A m}^2$ and a 20 MV electric potential...	51
Figure 35: Percent area increase as a function of the ratio between the particle energy and electrostatic potential.	52
Figure 36: 3D plot of particle trajectories colored to indicate proximity to origin (red is closer, green farther) [3].....	55

SUMMARY OF NOMENCLATURE

NOTE: All units are in the SI standard if unspecified

F – Force	γ – inverse Lorentz factor
q – fundamental unit of charge	λ – magnetic latitude
E – electric field	c – speed of light
v – velocity	C_{st} – Störmer characteristic length
B – magnetic field	R – particle rigidity
m – mass, rest mass	V – volume, voltage potential
g – gravitational acceleration	K_p – Particle kinetic energy
t – time	C – capacitance
r – position, radius	Q – total charge
e – unit direction	ϵ_r – relative permittivity
Ω_c – cyclotron frequency	ϵ_0 – permittivity of free space
r_c – cyclotron radius	K_{el} – elliptic integral of the first kind
r_s – solenoid radius	E_{el} – elliptic integral of the second kind
μ_0 – magnetic permeability of free space	$A_{old,new}$ – compared areas of Störmer region
M – magnetic dipole moment	PD_{Area} – percent increase in Störmer area
n – number of solenoid turns	
τ_g – gyroperiod or cyclotron period	
I – current	
r_{St} – Störmer radius	

CHAPTER I

INTRODUCTION AND GENERAL INFORMATION

The hybrid radiation shield concept, consisting of an unbalanced positive electrostatic potential barrier, in green, and a current-carrying superconducting solenoid, in blue, is shown in **Figure 1** and **Figure 2**. The following attempts to develop a good understanding of the motivation and background behind this concept.

1.1 Motivation

Active and passive particle radiation shielding for humans in space is currently considered by many to be a very difficult, if not impossible, concept to implement fully. For example, NASA's own radiation shielding program has largely shifted towards a bio-medical solution. This bio-medical solution appears to be an option only after further development in cancer treatment, due to the probability that one in ten men and one in six women will likely develop a malignant tumor from interplanetary radiation exposure during a typical one year Mars mission [1]. Also, the invention of drugs that properly combat high-dose radiation sickness is required to survive a solar particle event, with ongoing active research in this area [1]. Passive shielding would always be an effective method if spacecraft were not mass limited. There appears to be little room for theoretical improvement toward developing a lighter and more effective passive shield; currently rendering this option impractical. Thus, active shielding exists as the most probable method for achieving a universal solution through engineering and technological advancement. The materials and processes required for a lightweight active shield are also necessary for advancement in many other fields. It is then advantageous to optimize the overall active shielding concept to coincide with technological advancement. Hybrid shielding (those using both

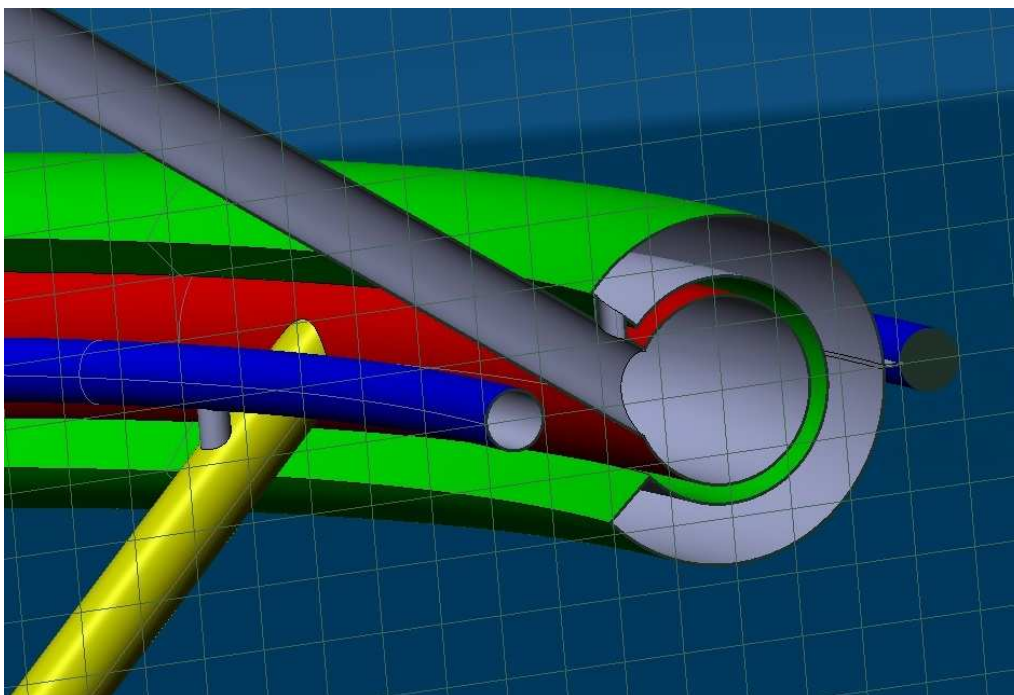


Figure 1: A cutaway view along the x-axis of the conceptual shield design. Red denotes the habitable zone, blue for the solenoid coils, green is the electric potential surface and yellow for the support structure

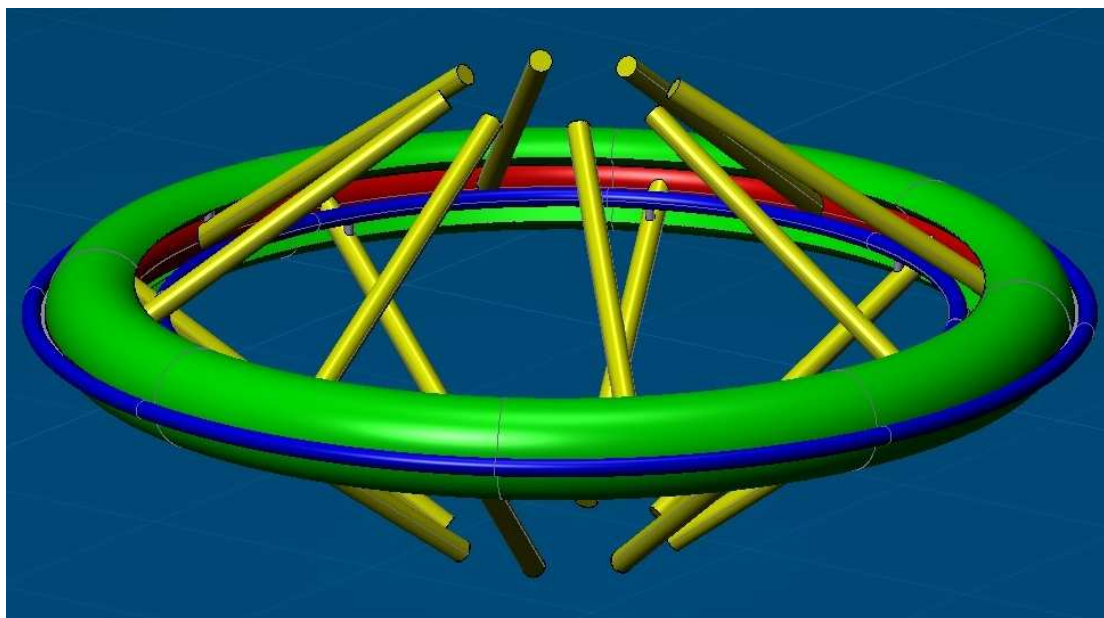


Figure 2: The full isometric view of the conceptual shield design. Red denotes the habitable zone, blue for the solenoid coils, green is the electric potential surface and yellow for the support structure.

electric potentials and magnetic fields) is considered by the author to be a promising concept, due to its high shielding efficacy to mass ratio as compared to other concepts. Because controlling particle trajectories in a magnetic dipole field with a complex electrostatic potential gradient is “not fully deterministic” [2], a quantification of how the electrostatic potential influences the Störmer exclusion region needs examination. This will enable an engineering design analysis to optimize the mass of a hybrid shield by matching the size of the particle exclusion region to the desired habitat geometry.

1.2 A General Overview of Radiation Shielding for Human Spaceflight

Several concepts exist to properly protect astronauts from the damaging radiation found in the harsh environment of space. There are two main categories under which all radiation shielding falls, namely active shielding and passive shielding. Passive shielding is a popular and effective method for lowering or eliminating human radiation exposure; being used in hospitals, nuclear power plants, research facilities, etc. It uses neutral mass to physically block harmful particles on the nuclear scale, which are colloquially termed “billiard ball” interactions. Active shielding has its own subsets which all utilize the charged nature of radiation; specifically electrostatic potentials, plasma and confined or unconfined magnetic fields. These concepts turn particles due to the Lorentz force relation.

Charged Particle Motion in an Electromagnetic Field

For an understanding of radiation shielding, a background in classical charged particle motion in electromagnetic fields is required. This type of motion is typically dominated by the Lorentz force with additional force due to gravity:

$$\vec{F} = q(\vec{E} + \vec{v} \times \vec{B}) + m\vec{g} \quad (1.2.1)$$

where q is the particle charge, \vec{v} is the particle velocity vector and \vec{g} is the gravitational acceleration vector. Note that this force only acts on charged particles. Electromagnetic waves are unaffected by static electric and magnetic fields in a vacuum. Let us first consider the case of a non-relativistic charged particle moving through a static, uniform electric field, E_0 , while neglecting other fields. The Lorentz equation simplifies to:

$$m \frac{d\vec{v}}{dt} = qE_0. \quad (1.2.2)$$

Integrating 1.2.2, the solutions for velocity and position at any time, t , are:

$$\vec{v} = \frac{q}{m} \vec{E}_0 t + \vec{v}_0, \quad (1.2.3)$$

$$\vec{r} = \frac{q}{2m} \vec{E}_0 t^2 + \vec{v}_0 t + \vec{r}_0. \quad (1.2.4)$$

Now let us consider the case of a non-relativistic charged particle moving through a uniform, static magnetic field, $B_0 e_z$, neglecting other fields. The Lorentz equation now simplifies to:

$$\frac{d\vec{v}}{dt} = \frac{q}{m} (\vec{v} \times \vec{B}). \quad (1.2.5)$$

Due to the cross product between the velocity and magnetic field vectors, we write equation 1.2.5 in the form:

$$\begin{pmatrix} \dot{v}_x \\ \dot{v}_y \\ \dot{v}_z \end{pmatrix} = \frac{qB_0}{m} \begin{pmatrix} v_y \\ -v_x \\ 0 \end{pmatrix} \quad (1.2.6)$$

where e_x , e_y and e_z represent a right-handed, orthogonal coordinate system and B_0 is in the e_z direction. The motion in x and y is coupled, resulting in a harmonic oscillation. Motion in z is unaffected by $B_0 e_z$, as can be seen here:

$$\begin{pmatrix} \dot{v}_x \\ \dot{v}_y \end{pmatrix} = \Omega_c \begin{pmatrix} v_y \\ -v_x \end{pmatrix}, \quad \dot{v}_z = 0 \quad (1.2.7)$$

where the cyclotron frequency (also referred to as gyrofrequency) amounts to:

$$\Omega_c = \frac{|q|B_0}{m}, \quad (1.2.8)$$

in units of Hertz. The cyclotron frequency describes the times per second the particle completes a full revolution, as it is moving in a circular path. The Larmor radius (cyclotron radius or gyroradius) describes the radius by which the particle moves, shown here:

$$r_c = \frac{v_\perp}{\Omega_c} \quad (1.2.9)$$

Figure 3 and **Figure 4** illustrates the helical motion and differences between positively and negatively charged particles. Note that the inclusion of relativistic motion is deferred to Chapter 3.

Current shielding configurations use unbound magnetic dipole fields, so it is necessary to give a description of a magnetic field due to an ideal dipole [3]:

$$\vec{B}(\vec{r}) = \frac{\mu_0}{4\pi} \left[\frac{\vec{M}}{r^3} + \frac{3(\vec{M} \cdot \vec{r})\vec{r}}{r^5} \right] \quad (1.2.10)$$

where μ_0 represents the magnetic permeability of free space. This is shown in **Figure 5**. Note that this is a good approximation for a current carrying loop. Equation 1.2.10 exists in Cartesian coordinates with the magnetic dipole moment, M , pointing in the positive e_z direction. The magnetic dipole moment is defined for a current carrying loop with turns, n , current, I , and radius, r , as:

$$M = \pi n I r^2. \quad (1.2.11)$$

Note that this magnitude points in the direction according to the right-hand rule for the motion of the current, I , around the loop.

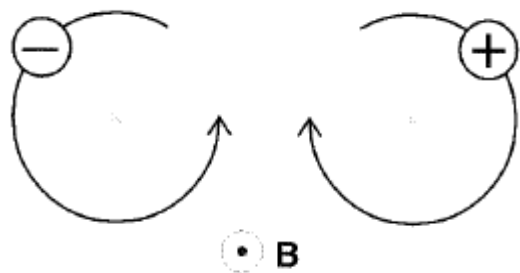


Figure 3: Circular trajectories of charged particles in a uniform and constant magnetic field, directed out of the page [5].

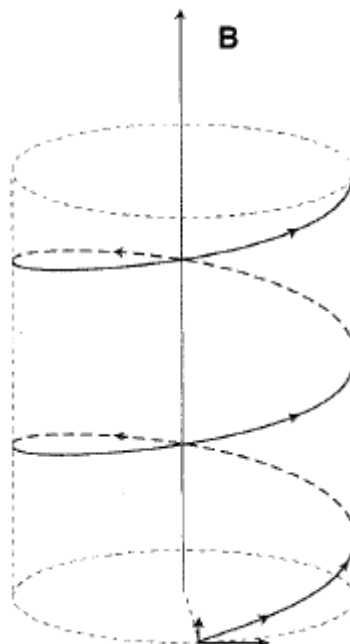


Figure 4: Helical trajectory of a negatively charged particle in a uniform and constant magnetic field along the z-axis [5].

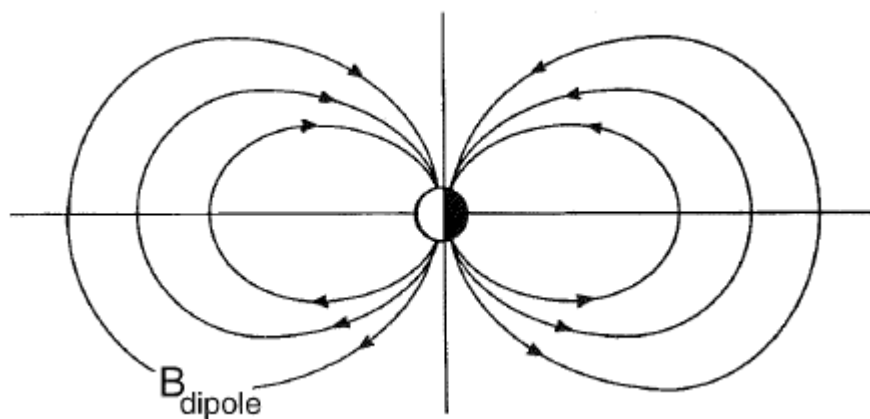


Figure 5: Magnetic field lines of a dipole [5].

An advancement on the understanding of magnetic dipole shielding involves the Störmer exclusion region [4]. The Störmer region simplifies particle shielding in a magnetic field by representing a volume that certain particles cannot access. This volume can then be used as habitable space for human occupants. The Störmer region is defined as the toroidal volume around the equator of a dipole into which particles of a specific energy are excluded. This can be seen in **Figure 6**, as shown in the r - z plane for the entire azimuth. Mathematically, Störmer defined the surface of the region as:

$$r_{St} = \sqrt{\frac{Mq\mu_0}{4\pi\gamma m v}} \frac{\cos^2 \lambda}{1 + \sqrt{1 + \cos^3 \lambda}} \quad (1.2.12)$$

where $\lambda = (\pi/2) - \theta$ is the magnetic latitude, $\gamma = \sqrt{1 - v^2/c^2}$ is the inverse Lorentz factor, m is the rest mass, c is the speed of light and r_{St} is the radial distance in spherical coordinates. The surface bounded region can be defined by a characteristic length, given here:

$$C_{st} \equiv \sqrt{\frac{Mq\mu_0}{4\pi\gamma m v}} = \sqrt{\frac{M}{R} \frac{\mu_0 c}{4\pi}} \quad (1.2.13)$$

for a given magnetic moment, M , and particle rigidity, $R \equiv \gamma m v c / q$. Note the actual shielded region is slightly smaller, with an outer radius at approximately $0.4 C_{St}$ for $\lambda = 0$ [3].

If the particle loses energy through various collision processes, it can become trapped in the magnetic field within a Störmer region that the particle was normally not excluded from. Once trapped, it will trend towards following the magnetic field lines and can undergo a mirroring process as shown in **Figure 7**. This entrapment of particles is shown in **Figure 8**, known as the Van Allen radiation belts. This is explained in depth in Gombosi's text [5].

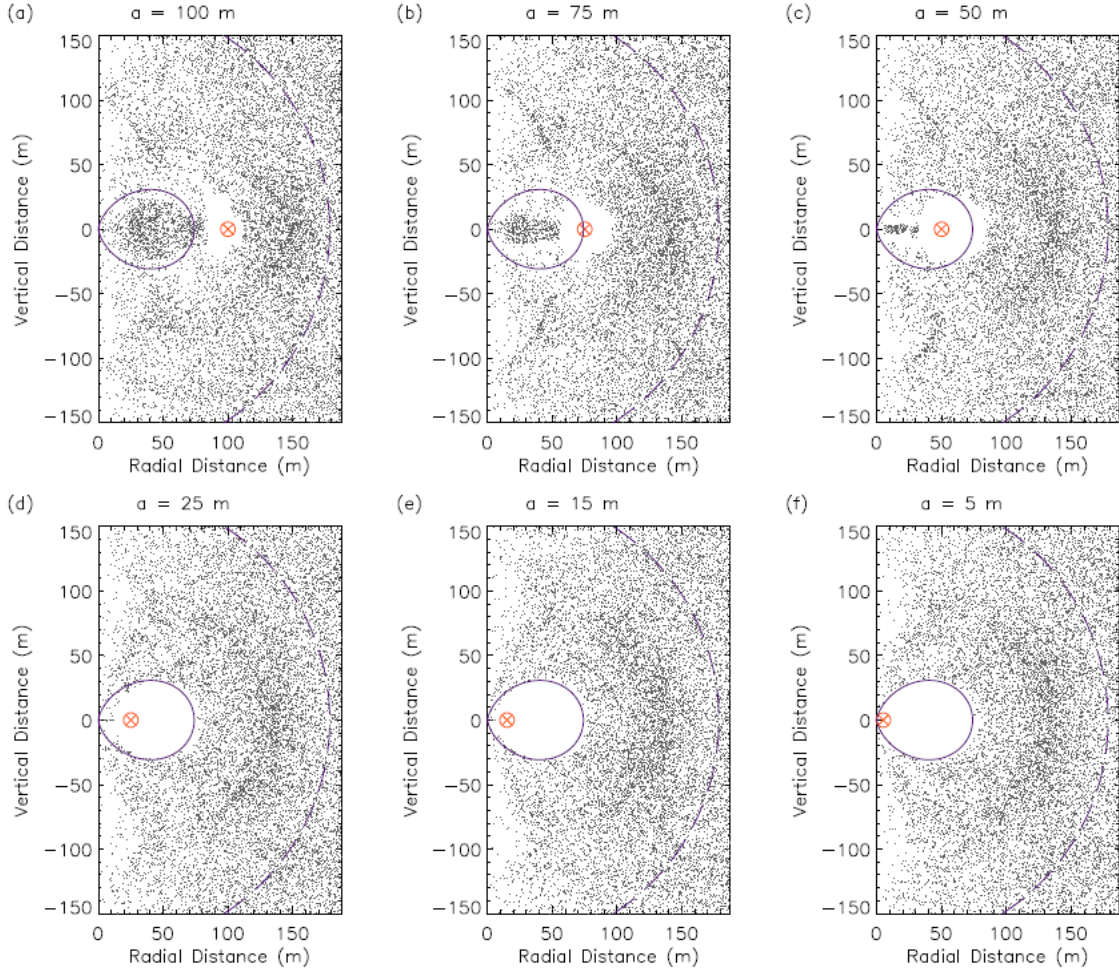


Figure 6: Plots of point of closest approach (grey dots) to the origin of 1 GeV Fe^+ trajectories in a magnetic dipole moment of $1.1 \times 10^{13} \text{ A m}^2$ for the entire 360 degree azimuth. Plots (a) through (f) denote a decreasing solenoid radius, a , for a constant magnetic dipole moment and particle energy. The solid line indicates the Störmer region for an ideal dipole. Note the deviation as the solenoid radius increases [3].

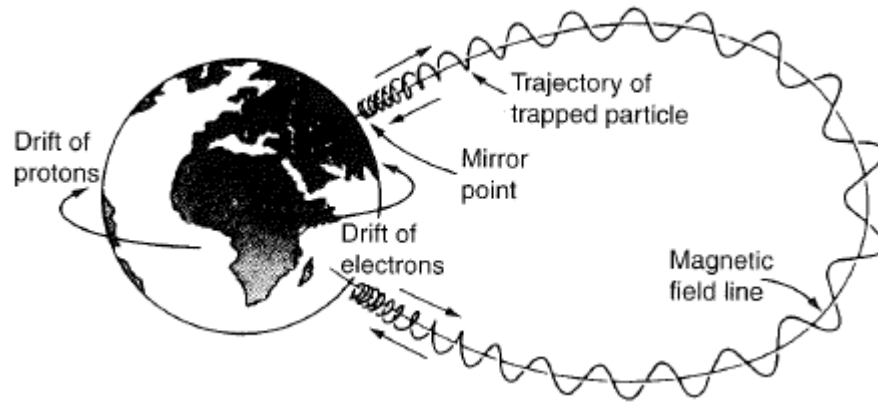


Figure 7: The motion of a trapped charged particle in Earth's magnetic field [5].

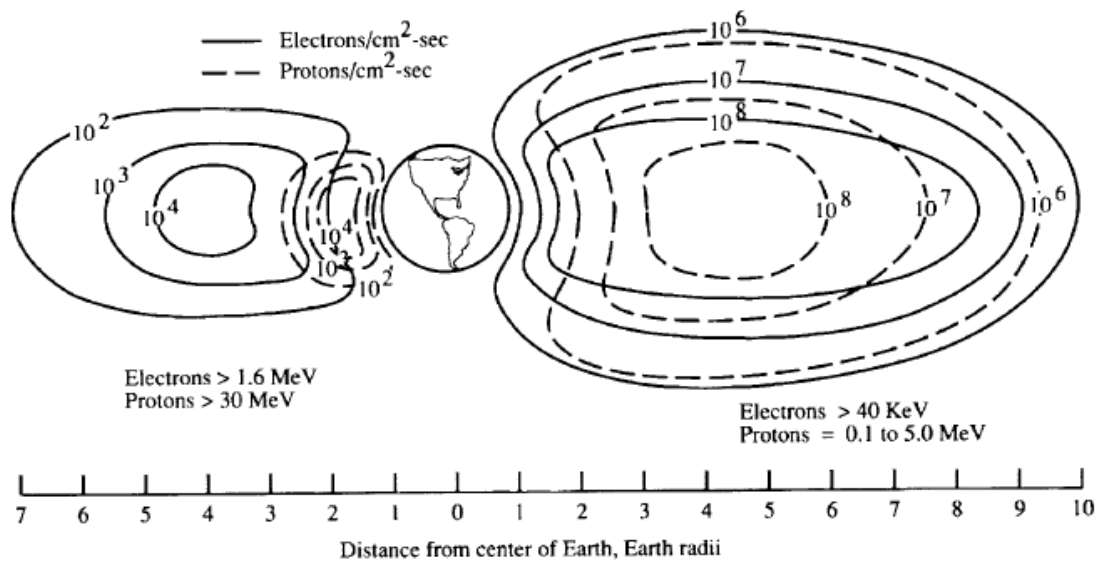


Figure 8: Location of proton and electron flux densities for the Van Allen radiation belts [26].

The Local Space Environment

It is appropriate to first examine the space environment for which all the outlined shielding concepts have been presented, as this will determine the constraints placed on any adequate system. Space exploration thus far has been limited to within the heliopause (the region of local space surrounding our solar system where solar plasma pressure matches interstellar plasma pressure), as the current farthest man-made object, the Voyager 1 probe, is still within the heliosheath. **Figure 9** shows a view of the solar system from the ecliptic north pole. In order to devise the appropriate shielding, identification of the particle and electromagnetic radiation most responsible for serious biological and electronic damage is necessary. High-energy particles found in the interplanetary region can be separated into three groups:

1. solar energetic particles (SEP) originating from the Sun,
2. galactic cosmic rays (GCR) originating from various sources outside the heliopause, and
3. heliospheric particles accelerated in the heliosphere by shock acceleration or ion pickup.

Solar energetic particles are produced largely from two solar events: coronal mass ejections (CME) and solar flares. These are often confused for one another but have different casual mechanisms and outcomes. CME's are large ejections of plasma from the sun inside regions of closed magnetic field lines generally found along the Sun's magnetic equator. This sudden release compresses ambient low energy plasma that previously left the Sun; much like a piston. This generates a shockwave of energetic plasma where the wavefront broadens as it propagates outward from the Sun. These tend to be largely composed of alpha particles within the CME, with a smattering of protons, free electrons and heavier nuclei. Solar flares are impulsive, short bursts of energy within the outer layer of the Sun, the chromosphere. This type of event begins with simultaneous flares in the microwave, visible and X-ray followed by type IV

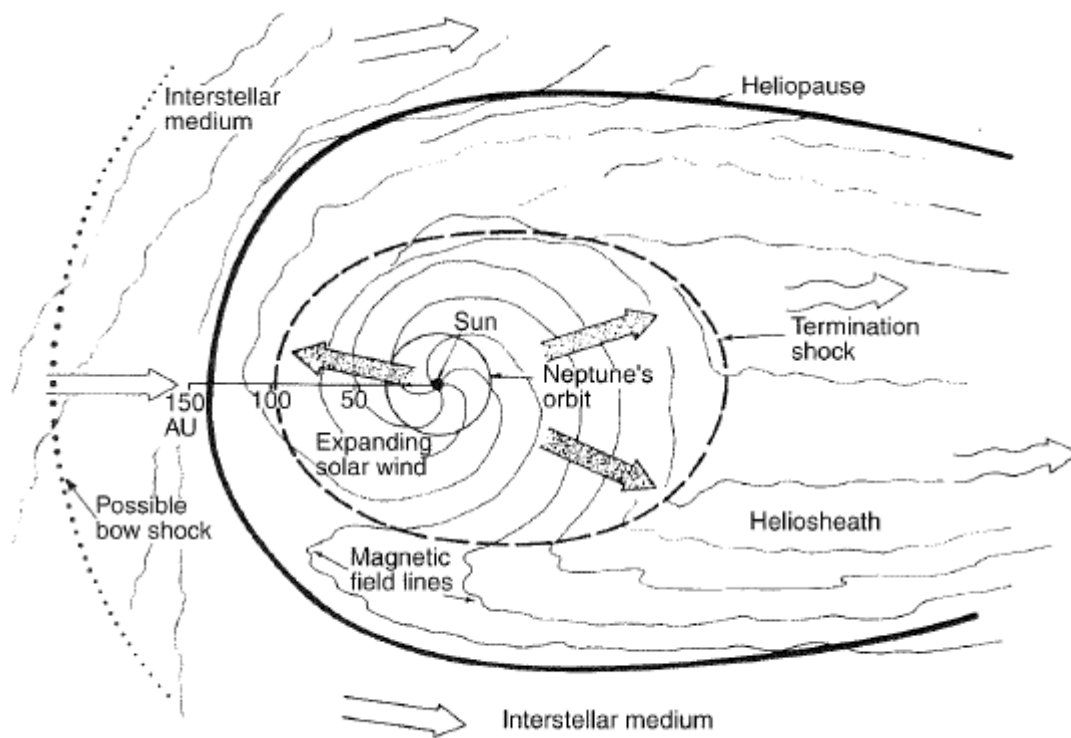


Figure 9: Schematic diagram of the heliosphere as seen from above the ecliptic north pole [5].

radio emissions that are longer-lasting. Note that the proton to alpha particle ratio varies greatly between flares. At Earth orbit, the particles initially follow the solar magnetic field lines but this quickly deteriorates into an isotropic velocity profile. Both of these solar events contain particles with energies from a few keV to several GeV. Note that this type of event carries a higher flux than all the proceeding energetic particle causes, but at lower energies [5].

Galactic cosmic rays are in fact not just photons but also high-energy nuclei and electrons that flow through interstellar space. The origins of specific GCR are still in question as particles below approximately 10^{15} eV are widely believed to come from galactic sources, whereas higher energy GCR above 10^{18} eV are thought to originate from outside our own Milky Way galaxy [5]. Also as a good general rule, GCR flux is essentially isotropic below 10^{15} eV [5]. Due to the fact that GCR is from sources outside the solar system, their influx depends on the outward flow of solar particles analogous to a pressure balance. GCR intensity therefore fluctuates inversely with the solar cycle on an 11 year basis. The solar cycle and GCR influx are both not stable, which leads to a general 22 year cycle of GCR intensity (for a more in depth look at how GCR modulates over time, refer to Gombosi's text). Refer to **Figure 10** for a good illustration of this phenomenon. The Bulk GCR energy spectrum has been measured throughout this cycle to be largely between 100 MeV to less than 10 GeV [5]. This consists of roughly 83% protons, 13% alpha particles (2 protons, 2 neutrons), 1% heavier nuclei (actually the most dangerous) and 3% free electrons [5]. Research has shown that this statement holds basically true for the bulk GCR spectrum up to 10^{14} eV [5]. Any information about the GCR composition above this has not been directly measured. **Figure 11** shows the flux at varying kinetic energies for the bulk spectrum. **Table 3** and **Table 4** show various solar wind parameters, found in Appendix A.



Figure 10: Monthly averages of the approx. 1 GeV galactic cosmic ray intensity observed by the Mt. Washington neutron monitor from 1954 through 1979. From Ref. [5], original plot by Ref. [24].

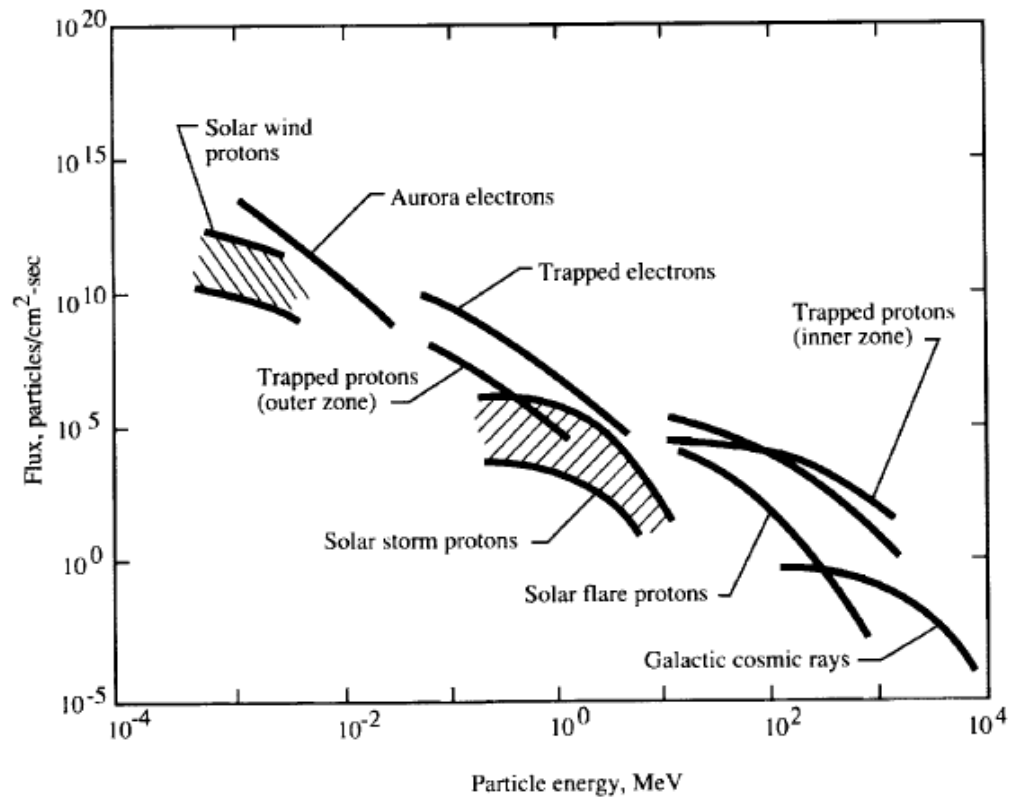


Figure 11: Plot of the particle energy flux density spectrum for the typical interplanetary medium [23].

The lowest flux of the three in near-Earth space, heliospheric particles carry some background as to our solar system's interactions within the local region of the Milky Way galaxy. The very local interstellar medium (VLISM) surrounds the heliopause and is moving roughly in the opposite direction of our sun-system velocity, with a relative speed between the two at about 26 km/s [5]. This gas is partially composed of neutral atoms which move rather freely inside the heliopause. Because these neutral atoms are relatively cold, at both thermal and kinetic energies, in comparison to the energetic particles a good approximation states that the relative speed between the interstellar neutral particles and the magnetized solar plasma is simply the solar plasma speed. Now, these neutral particles can be ionized by several mechanisms: photoionization, charge exchange with other ions, or electron impact. Once ionization occurs these young ions are still at rest, but are then gradually accelerated by the motional electric field from the high-speed solar flux. These ions can reach speeds up to eight times that of the local solar wind experiencing an inward drift towards the sun [5]. **Figure 12** shows this velocity distribution normalized by the average solar wind velocity. The second type of heliospheric particle was found unexpectedly and extends to at least 60 AU, indicating that these are from extrasolar sources [5]. These were summarily termed anomalous cosmic rays and exist at energies between 1 MeV/nucleon to 30 MeV/nucleon, which are relatively low energy compared to GCR and SEP [5]. Note that this is an ongoing area of research, as the consensus suggests these anomalous cosmic rays are simply highly accelerated pick-up ions [5]. The mechanisms which could theoretically accelerate these ions are not within the scope of this research, with potential solutions in Gombosi's text.

Radiation Dosage Limits for Human Space Travel

Making a case for human radiation shielding in space is based on survivability and mission capability, (i.e. can astronauts perform mission tasks and return with a reasonable life expectancy). It has been concluded that a stochastic increase

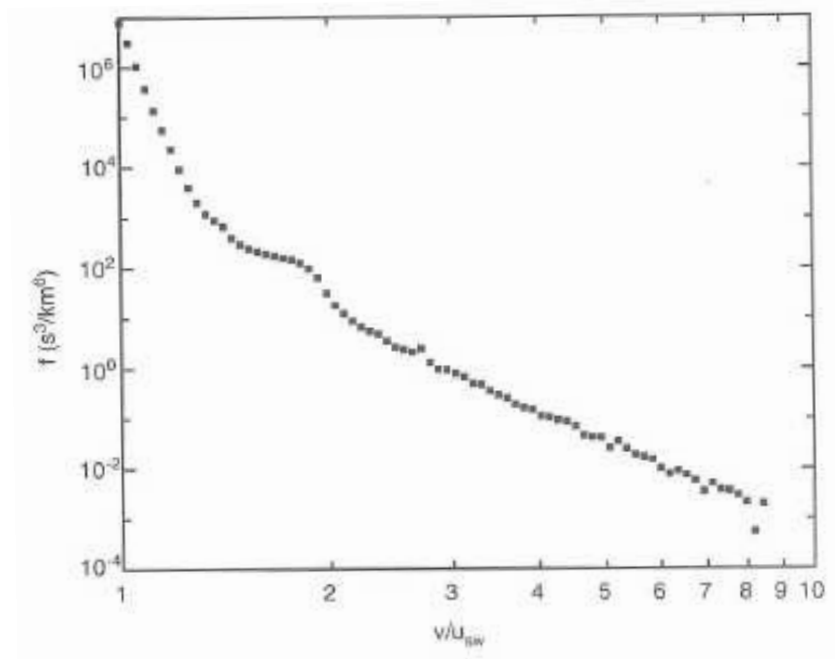


Figure 12: Pickup proton velocity as measured by the Ulysses spacecraft. From Ref. [5], original plot from Ref. [25]

in the cancer rate of astronauts (males above 35 and females above 45 years old) of a mere 3% can be deemed mission critical, due to the danger of an astronaut developing cancer or an equally nefarious radiation induced medical condition. Without nearby modern medical treatment, such an event could place the entire mission at risk [6]. As such, the numbers in **Table 1** are guidelines for radiation exposure based on an average length mission to Mars. This was pulled from various legislation safety requirements and relevant literature [7]. This sets a good framework for the acceptable dosage limits for continued human scientific research and exploration in space. To demonstrate the locality dependence, **Figure 13** gives a basic overview of the exposures existing at specific regions both on Earth and in space. One can then extrapolate from these two number sets the shielding efficacy for a given mission (i.e., lunar surface colony or Martian voyage).

Space Radiation Shielding: Passive Shielding

Passive shielding is by far the most prevalent form in use today for terrestrial purposes, as weight is not an issue. Most of these shields are composed of dense and/or cheap material (e.g. water, lead and concrete) to provide protection from all forms of laboratory, medical and nuclear power born radiation. These descriptors are useful due to the nature of radiation as it interacts with a medium. Any particle or electromagnetic wave clearly encounters no resistance when traveling through an absolute vacuum. Resistance only occurs when a medium exists to attenuate the traveling photons or particles. The amount of attenuation experienced by the photon and shielding of an energetic particle is directly dependent on the properties of the blocking element or molecule and the energy states of the radiation, which is determined in general by the particle's velocity (typically expressed as the relative kinetic energy equivalent in electron-Volts) and photon's frequency (in Hertz). Good macroscopic metrics to define blocking capability consist of the density and thickness of the shielding material in the incident direction of radiation. These are good descriptors because the material

Table 1: Proposed dose equivalent limits (in Sievert) for a mission to Mars [6].

	1 minute	1 hour	1 day	1 month	1 year	Mission
Warning	3 μ Sv	0.8 mSv	10 mSv	0.20 Sv	0.40 Sv	0.80 Sv
Alarm	3 warnings	1.0 mSv	12 mSv	0.25 Sv	0.50 Sv	1.00 Sv

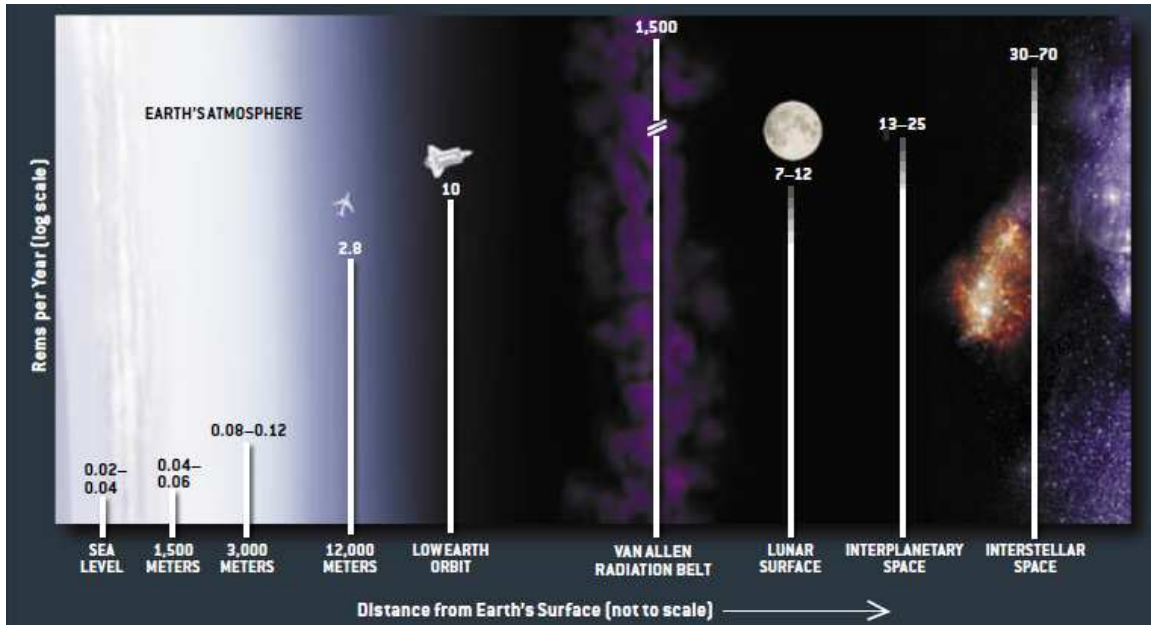


Figure 13: Several locations with corresponding average dosage per year for humans, in Rems [1].

needs to continuously collide with the incident radiation, as per the Coulomb force on an atomic scale, until all particle kinetic energy is dissipated. The energy dissipates after each collision by generating additional charged particles at lower energy states than the previous collision (For a more rigorous examination of photon and particle interactions with solid, liquid and gaseous media, please refer to Watkins thesis [8]). Clearly, the denser and thicker the material in general, the higher energy radiation it is able to absorb. However, certain materials combined with high energy radiation can actually be harmful due to the additional particle and photon generation. As one example, high frequency gamma rays mostly generate lower energy X-ray Bremsstrahlung (literally “braking radiation”, it is a continuous spectrum of photons emitted by decelerating a particle) as they cascade down from high energy levels due to electron collisions. If the material is not thick enough to absorb this additional radiation, it can be shown that this is more damaging than no passive shielding. A good analogy would be the shrapnel generated by a high velocity bullet piercing through thin armor. The bullet still pierces the target but is now accompanied by the additional shrapnel. In order to combat this “shrapnel” radiation, materials consisting of mostly protons within their respective nuclei with well bound electrons have been shown to produce less harmful by-products, such as liquid hydrogen, helium or ethylene [9].

Now, please note the definite contrast between the previous earth-based system and an orbiting shield, as the customary terrestrial-based shield needs to contain harmful particles and radiation from escaping a “control zone” where the latter must maintain a livable volume inside a harsh exterior environment. This can be extended to the difference between the two systems as a whole for each shielding method. This presents a unique situation for space based systems because the volumes considered must enclose a large living space while still maintaining a thickness capable of stopping high energy particles. Taking a

simple sphere with a volume of $V = \frac{4}{3}\pi r^3$ clearly shows the disadvantage which plays into needing to fill an external, rather than internal, volume with shielding material on orbit, where mass carries a significant cost.

Active Shielding

Transitioning to active shielding, please note that the author has yet to find a concept tested outside of a controlled laboratory environment. All designs through 1999 were still within conceptual phases of development [10].

Theoretical electrostatic shield designs are largely based on technologies which enable large capacitors to function, as it can be shown that large electrostatic gradients are required to block heavy, high-energy ions. Electrostatic shield design consists of two distinct groups:

1. dipole plates/spheres and,
2. unbalanced potential bodies [11].

A dipole can be in virtually any arrangement (two capacitor plates, spheres at the ends of a shaft or “dumbbell”, spheres in a branching “tree” structure), typically with a negative outward potential due to the consideration for both ambient “quiet time” and energetic GCR electrons. If the positive potential was outward-facing, the system would attract electrons and accelerate them much more rapidly than the ambient thermal ions would with the standard negative outward potential, due to the significantly lower electron mass. Also, the electrons would then impact the positive potential spheres, neutralizing the charge and diminishing the ability to shield positive ions. It has been theorized that the magnitude of current flow required to then maintain a positive potential would be enormous and completely outside the capability of most terrestrially-based power plants, let alone a space-based system [11]. A conceptual dipole sphere tree is shown in **Figure 14** with its corresponding potential in **Figure 15**. Unbalanced potential bodies, on the other hand, always present a single outward potential; being either positive or

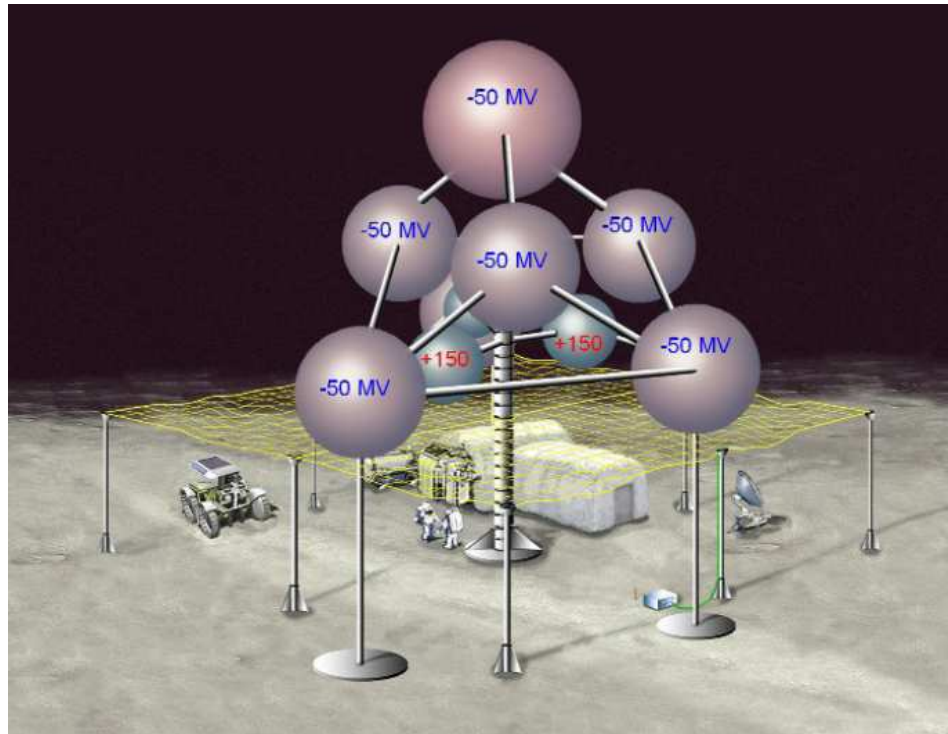


Figure 14: Electrostatic shield concept for lunar base [2].

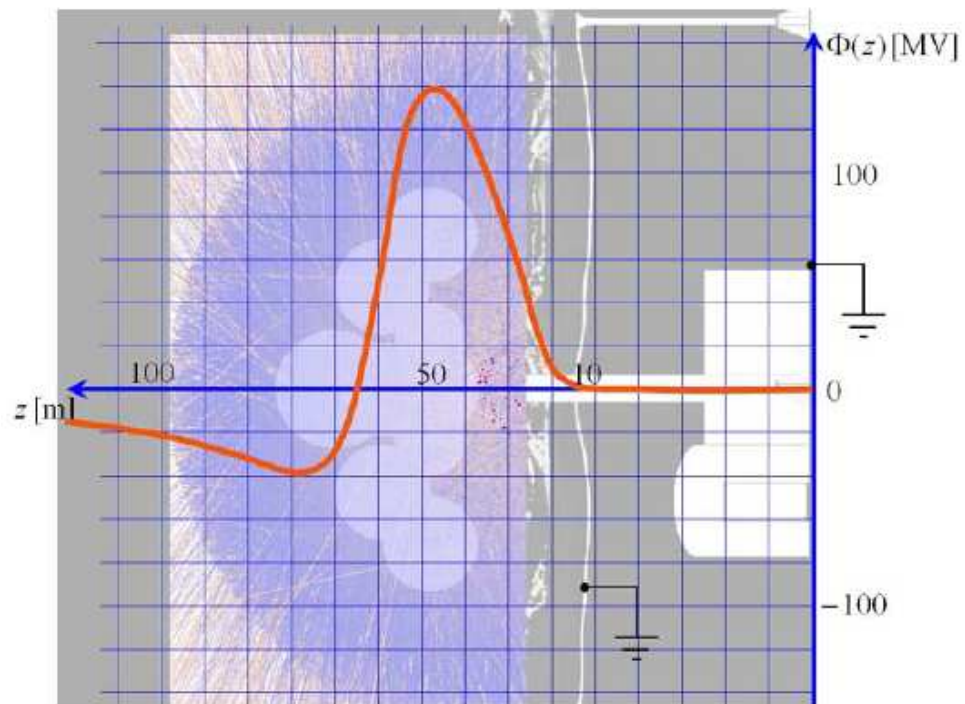


Figure 15: Electric field strength along z-axis for Figure 14 [2].

negative. This presents the same problem as previously mentioned with inflow of the opposite charged particle impinging on your charged body. The only known method to combat this flow of particles is to couple this system to a solenoid-generated magnetic field. This will be discussed more in-depth in the following section concerning hybrid shield systems. There are modern constraints on electrostatic shield systems due to several factors:

1. the dielectric breakdown strength of the materials,
2. the limitations on high voltage power supplies (current power supplies are limited to 20 MV) [2], and
3. the structural limits of the considered materials which must not be surpassed by the internal coulomb forces between charged bodies [2].

Kapton is a good example of a dielectric material commonly used due to its high dielectric breakdown voltage of 291 kV/mm, along with a reasonable tensile strength-to-weight ratio [12]. As an endnote, there are no known major biological issues associated with strong static electric fields, mainly because no studies have taken place using field strengths on the order required. Minor physiological effects are noted as skin surface charge densities increase, leading to raised hair follicles (electrons accumulate in the protein-dense structure and repel the negative surface charge) and the possibility for spark discharges. Also, the possibility for ionization of biological molecules has not been evaluated at the voltage levels occurring in electrostatic shielding [13].

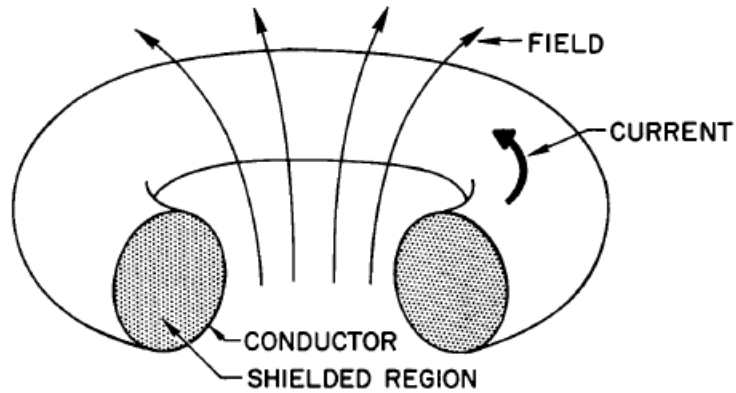
Static magnetic shielding can be generalized into two categories: unbound and bound. They both are composed of some arrangement of conducting material wrapped into a solenoid or system of solenoids, with the material existing as the major constraint. At all practical shielding levels for space-based applications, some type of superconducting infrastructure is required in order to maintain viable levels of current without tremendous heat and energy loss. This forces a cryogenics component on all current designs in order to maintain superconducting temperatures [8] (e.g., a liquid helium/nitrogen refrigerant cycle,

magnetocaloric metals, etc.). The type of material greatly influences the temperature that the system must be maintained in order to remain superconducting. Also, the maximum realizable current density changes from various factors in the material's structure. The higher the current density to mass ratio and superconducting temperature of the material, the more valuable it becomes in comparison. Again as an endnote, exposure to magnetic fields must be minimized as deemed appropriate by the WHO. Movement in a strong magnetic field, on the order of 2 T, causes electrochemical effects in the photoreceptors in the eyes and acidifies the saliva with general nausea and dizziness from extended exposure. It is thought that larger magnetic fields could create detrimental flow effects in the bloodstream of a human, especially near the heart, potentially causing fatal side effects [13].

Unbound magnetic shielding is comprised of either a single solenoid or solenoids that allow their magnetic field lines to wrap back around their magnetic equators (north wrapping back to south), as in a pure dipole field. This is an effective working definition, as many configurations are possible. The most common consist of a dual solenoid that is both concentric and coplanar, with one having a slightly larger radius. **Figure 16** shows an unbound concept from the mid 1960's. **Figure 17** demonstrates a more modern concept. This allows for a small region between the solenoids that is free of strong magnetic fields. This configuration is a good approximation for an ideal dipole when the radius of the solenoid is small compared to the region requiring shielding [3]. This system blocks particles by creating a magnetic field at large distances from the protected region, affecting a particle's trajectory well before it approaches the shielded region. The Earth's magnetosphere is essentially an unbound magnetic shield that blocks a moderate amount of particle radiation at low magnetic latitudes before they impact the atmosphere.

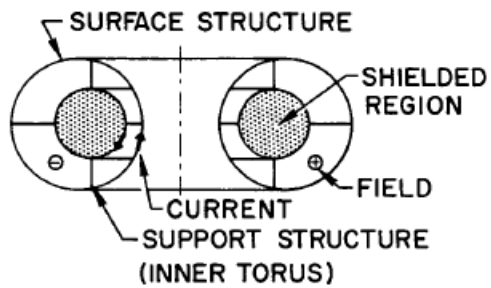
I UNCONFINED FIELD

EXTERNAL FIELD TOROID GEOMETRY (HOLLOW CONDUCTOR)



II CONFINED FIELD

DOUBLE TORUS



HYBRID TORUS

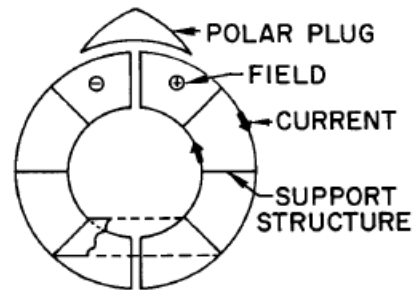


Figure 16: Three basic configurations for magnetic shielding [27].

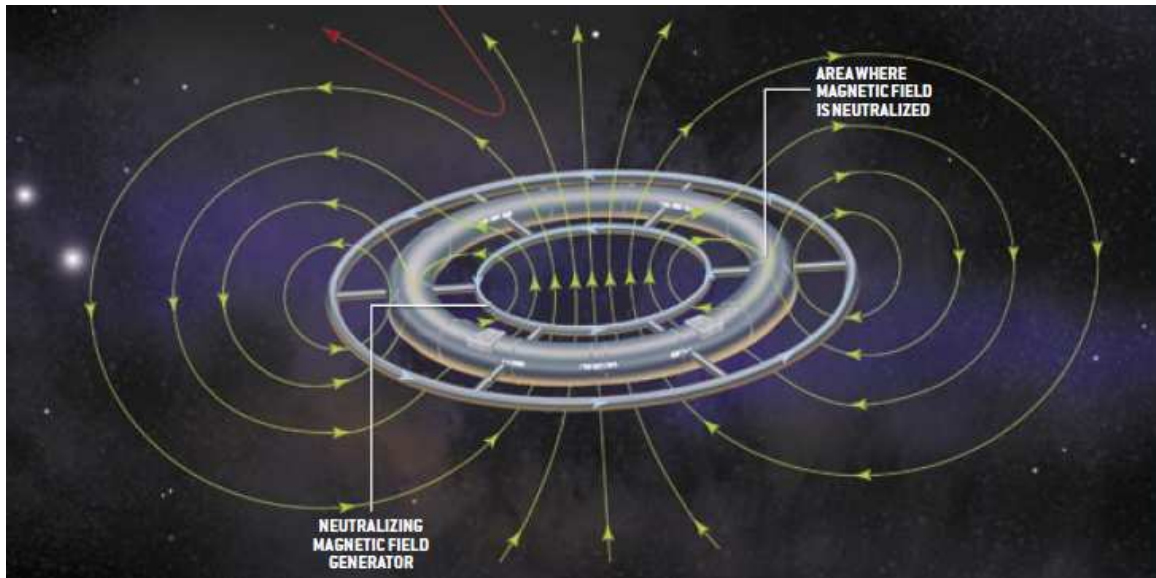


Figure 17: Basic unbound dipole conceptual design [1].

Bound magnetic shields consist of a system of solenoids whose magnetic field lines flow into other solenoids over a looped arrangement, thereby mostly containing the magnetic fields within their interior radii; usually in the shape of a torus. **Figure 16** and **Figure 18** illustrate some simple configurations with highlighted or marked magnetic fields. This system blocks particles by generating a very intense magnetic field within the solenoid radius, allowing for particle turning from the small gyroradius.

Plasma shielding can be defined as a system that utilizes a mass of ionized particles contained by electromagnetic fields to repel incident radiation. This was first thought to consist of only a positive outward potential, but this attracts ambient electrons. A magnetic field was then added to turn the attracted electrons. The electrons can become trapped in the field, similar to the Van Allen belts, and orbit the system. It was thought that the captured electrons would help shield incident proton and ion radiation. However, the electrons continue to accelerate until impacting the potential surface. This represents a negative current flow, gradually neutralizing the electrostatic shield. This is better characterized as a hybrid shield because the electrons do not produce the main shielding effect. Advances in electron containment research have enabled “pure” plasma shields. One modern plasma shield concept uses controlled radio-frequency photon emission to generate a rotating magnetic field, trapping electrons in a stable orbit without any electric potential present [14].

A hybrid shield uses both electromagnetic fields to turn incident radiation, resembling early plasma shields. Therefore, modernization of this system would add passive shielding through the use of trapped current absorbers at the magnetic poles. These absorb electrons before they accelerate and impact the positive potential surface, preventing neutralization. This would consist of low atomic number elements or molecules (such as helium, hydrogen, water or polyethylene) to prevent collision induced bremsstrahlung, identical to effective

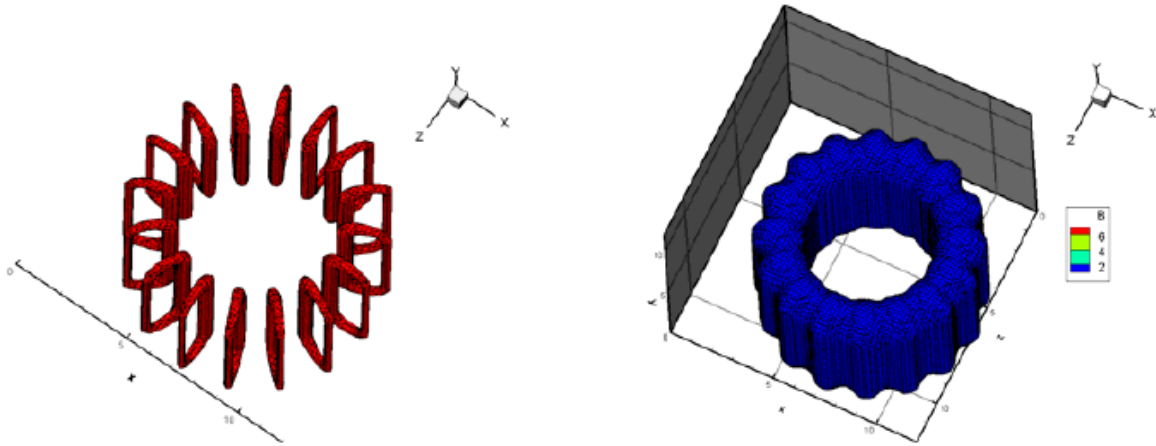


Figure 18: Bound magnetic shield without y-axis “end plugs” (left) and corresponding magnetic field strength surface, shown for 2 Tesla (right) [28].

passive shielding. Modern hybrid shields would then use all three major methods to block particle radiation.

Compare and contrast: Active Shielding

Each concept comes with both advantages and disadvantages based on current technology levels. Passive shielding has the advantage of effectively shielding against all forms of ion, proton, neutron, electron and photon radiation (photons and neutrons are not known to be affected by electromagnetic fields) but is too massive to be launched into space [1]. This is determined by payload sizing on earth-to-orbit transport, which is currently too small to accommodate passive shielding. If payload sizes increased, passive shielding would once again become a feasible option.

Active shielding concepts vary in necessary mass, power and energy, where the later two can be described as functions of mass. An effective active shielding system therefore has both low power and energy consumption while remaining effective at turning incident radiation. Electrostatic shields can be very lightweight, but generate a current influx based from their opposite outward potential [15]. They also are voltage limited, preventing the system from blocking all necessary radiation. Magnetic shields tend to be heavier than electrostatic shields, but do not attract current and are capable of blocking necessary particle radiation with current technology.

Now from an engineering standpoint, bound and unbound shields differ in a few distinct ways. Bound shields offer an advantage by virtually eliminating intense magnetic field issues within other parts of a spacecraft. A ship flexing, even slightly, within its own magnetic field gradient could generate enough current to damage onboard electrical hardware outside the human habitable zone (it is clearly impractical to completely shield all parts of a spacecraft sized for interplanetary travel). Therefore, electrical systems would require both radiation

and magnetic “hardening” outside the habitable region. Bound shields, however, require a more intense magnetic field to produce comparable shielding to unbound shields, thereby necessitating larger currents. Larger currents require either larger or better superconductors which scale up the system in cost and/or weight.

Plasma shield concepts are the lightest and require the least amount of energy, but are experimentally unproven as to their actual shielding efficacy and ability to control electron orbits [15]. Hybrid shields attempt to maximize the advantages and minimize the disadvantages of both electric and magnetic shields. They are both lighter than a pure magnetic shield and more capable at blocking the required radiation than electrostatic’s [11], while holding experimental evidence confirming electric and magnetic shielding potential over plasma shields [15].

CHAPTER II

LITERATURE REVIEW

2.1 Electromagnetic Shielding Research Review

Shepherd and Kress's Results [3]

Recent research by Shepherd and Kress [3] examined the question of whether a deployed shield provides an internal protection region. This was in direct contrast to older claims by *Cocks et al.* [16] that a large deployable shield was more effective at creating an internal shielded region. Shepherd and Kress [3] show, from an intensive numerical computation on varying energy levels of charged protons and iron nuclei, that a shielding region only exists when the solenoid radius is much smaller than the proposed characteristic Störmer length, C_{st} , as previously defined by Störmer's theory. The results from Shepherd and Kress [3], found in **Figure 6**, will be directly compared to the numerical results of this thesis as a test case for validation of the author's code. They finally conclude that they are in agreement with Parker [1], [9] and others that doubt generated magnetic fields of the magnitude required to shield are feasible, without specifically indicating the reasons why.

Cocks and Watkins' Analysis and Results [16], [8]

A very thorough thesis presented by Watkins [8] provides good insight into direct engineering issues related to the production of a deployed unbound magnetic shield. The thesis provides a clear basis for defining the mass of the solenoid wire as a function of its current density and radius. It also defines good assumptions for the properties of a superconducting candidate for the wire material, with a 1×10^9 Amps/m² max current density and 8 g/cm³ mass density [8]. The study by *Cocks et al.* [16] carries Watkins [8] as the second author, with the basis of the study clearly related to Watkins' graduate research in deployable

superconducting coils. Both studies present basically the same idea; that a large radius superconducting coil deployed in space will be lighter and significantly less energy intensive than a comparable small radius coil. They also assert that a region of exclusion defined by Störmer's relation exists for the coil. This was shown numerically to be incorrect by Shepherd and Kress [3]. Note that there is a region of exclusion from the magnetic field of a large radius deployable coil for specific particle energies, shown in **Figure 6**, only that it exist under a differing size and shape. This result would suggest that the deployable coil could then be used to shield an exclusion region, but it will be smaller than the comparable Störmer's relation would suggest. Therefore, a new analytic solution is required to properly define the exclusion region as a function of the coil's radius.

Buhler's Results [2], [11]

An analysis by Buhler [2], [11] for a lunar based radiation shield lays current groundwork for pure electrostatic and hybrid shield concepts. His conclusions from the final report [2] seem to disagree from his earlier results, as it is clear from **Figure 19** that the hybrid shield is a more effective solution from a pure shielding standpoint. Buhler [2], [11] asserts that including a solenoid generates problems that literally outweigh the benefits, as the required additional weight nullifies any advantages. These conclusions are drawn without any attempt at showing weight comparisons between any of the shielded systems. His conclusion also states that electrostatic shields carry problems from incident electron bremsstrahlung, whose impacts are clearly shown on a pure electrostatic shield. These impacts could generate x-ray and gamma ray photons that are potentially more damaging than the electrons themselves. Buhler [2], [11] does state that this is an area of ongoing research, proposed for further studies because particle motion in a combined magnetic dipole field with a complex electrostatic potential gradient is "not fully deterministic" [2]. This result and conclusion were the direct motivations for this thesis. Relatedly, motion of a charged particle trapped in a magnetic dipole field alone can be described as

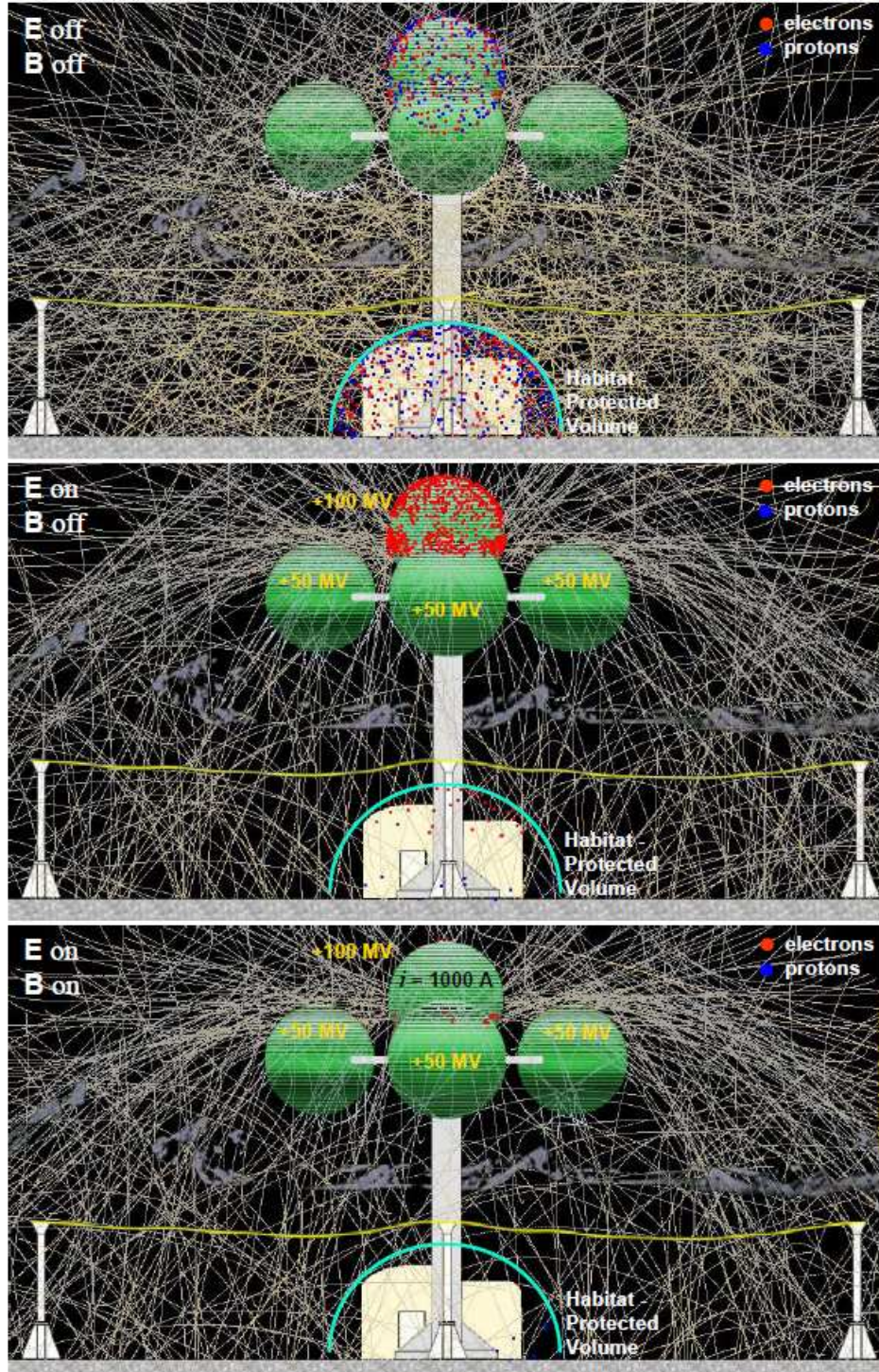


Figure 19: Comparison between pure electrostatic potential (middle) and a hybrid system (bottom) representing particle collisions with the central potential surface and habitat volume [11].

deterministic chaos [17]. This is defined as an “irregular or chaotic motion that is generated by nonlinear systems whose dynamical laws uniquely determine the time evolution of a state of the system from a knowledge of the previous history” [18]. Motion in an electric and magnetic field is also deterministic, defined that “there exists a prescription, either in terms of differential or difference equations, for calculating (its) future behavior based from given initial conditions” [18]. Buhler [2], [11] appears to attempt to relate this concept by his statement “not fully deterministic” in ref. [2].

CHAPTER III

METHOD OF ANALYSIS

3.1 Numerical Technique

The numerical technique employed herein to analyze the theorized shielding system was written in MATLAB R2009b (code in Appendix B) and simultaneously ran on two personal desktop computers. This code performs a randomized initialization of position and velocity unit vectors in a Lagrangian reference frame, whereby each particle is simulated individually without influence from other particles. Each particle is injected at a specific energy (100, 150 MeV and 1 GeV) and radial position (50 km). Two cases were evaluated at each particle energy, using 2×10^4 particles in each. The first case applied only the dipole magnetic field (magnetic moment of $1.1 \times 10^{13} \text{ A m}^2$), where the second added an electrostatic potential (20 MV). The 20 MV electric potential was chosen because this is the maximum output voltage of existing power supplies [2], meant as a form of limit testing for current technological capabilities. One pure magnetic field simulation was evaluated with $5 \times 10^4 \text{ Fe}^+$ particles at 1 GeV for result comparison. The code itself consists of three main components: the initial setup, the electromagnetic field solver and the particle mover.

Initial Setup

The code configuration consists of both an electric potential barrier and a current carrying solenoid surrounded by a spherical surface on which particles are injected. This conceptual shield design can be seen in **Figure 1** and **Figure 2**, where red denotes the habitable zone, blue the solenoid coils, and green is the electric potential surface. Many initial conditions and methods for this computation were directly taken from the previous study by Shepherd and Kress [3] to allow for direct comparisons. These were:

- the dipole magnetic moment ($1.1 \times 10^{13} \text{ A m}^2$),
- type of simulated particle (Fe^+),
- number of simulated particles (5×10^4 . Note 2×10^4 was the main value),
- timestep as a percent of the gyroperiod,
- initial particle radius (50 km),
- and particle energy (1 GeV. Note that 100 MeV and 150 MeV were also used).

Iron ions are chosen as the shielding benchmark due to their highly damaging nature (one iron ion does 676 times the damage of a proton at the same energy [1]) and significant interstellar flux. The only known direct deviation from Shepherd and Kress [3] was that the solenoid's magnetic field was calculated from an exact integral formulation for a current carrying solenoid.

Particle positions and velocities unit vectors are initialized by a uniform distribution of random numbers. The position is generated as a function based on the initializing radius, while the velocity unit vectors are limited to a hemisphere directed at the origin. The method of particle randomization used here is packaged into MATLAB as the default random number generator in R2009b, which uses the Mersenne Twister algorithm. This specific algorithm was developed by Matsumoto and Nishimura [19]. Each random number is used twice, with the first particle's position being generated by the first number and velocity unit vector by the last. The numbers then converge inwards, with the middle particle (on a run with an odd number of particles) using the same number twice. Each particle is injected at a kinetic energy of 1 GeV, as it is common in particle physics to use this unit. The energy is converted into a velocity magnitude by the equation:

$$|\vec{v}| = \sqrt{c^2 - \frac{c^2}{\left(\frac{K_p}{mc^2} + 1\right)}} \quad (3.1.1)$$

and then multiplied by the randomized unit vector to generate the particle's full velocity vector.

The initial geometric setup was developed mainly for the discrete monopole torus, because the solenoid calculations only rely on a single set radius for the loop. In order to convert a toroidal surface into a discrete monopole system, three rings were generated with the positive charge point monopoles located along the radius as shown in **Figure 20** and **Figure 21**. This consisted of 20 equidistant points per ring. The ring radii were equated to the solenoid loop radius, at 25 m. A positive electrostatic potential was applied as referenced from the rest of the spacecraft, at ground potential. An equation was derived which equated voltage to number of fundamental charges (for use in the electric field solver) for each monopole. The number of charges per monopole was set to match an identical potential found on a sphere under self-capacitance. The derivation begins with the definition of capacitance:

$$C = \frac{Q}{V} \quad (3.1.2)$$

which for a hollow conducting sphere with radius r_s referenced to a concentric sphere at an infinite radius is [20],

$$C = 4\pi\epsilon_r\epsilon_0r_s \quad (3.1.3)$$

Equating 3.1.2 and 3.1.3, then rearranging gives,

$$Q = 4\pi\epsilon_r\epsilon_0r_sV \quad (3.1.4)$$

where ϵ_r is approximately 1 for the interstellar vacuum. An answer is returned (in coulombs) that is then converted to numbers of elementary charge. This is used in the field solver to determine the E-field at any point in space.

Electromagnetic Field Solver

The electromagnetic fields are solved in two steps. The magnetic field is solved first from the exact integral of a current carrying loop according to the Biot-Savart

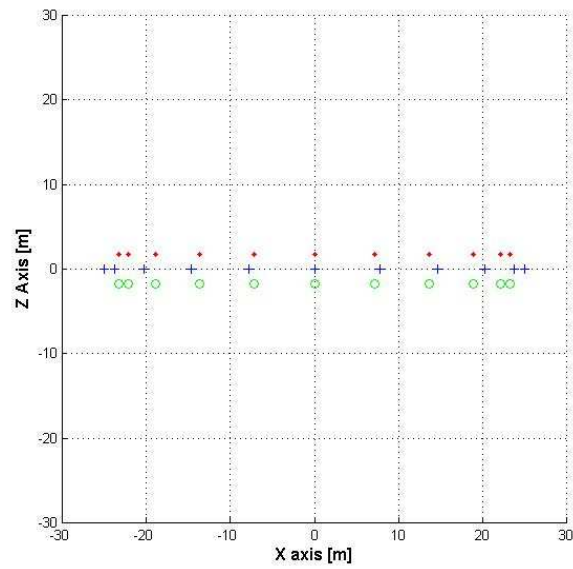


Figure 20: z-x plot of the electric potential surface as discretized into point charges and generated in three rings. Note that each point holds the same number of fundamental charges.

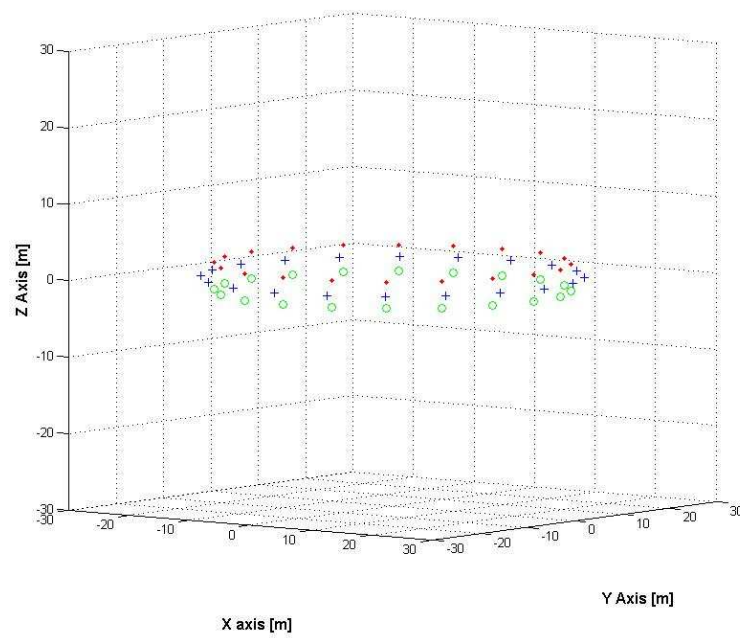


Figure 21: 3D plot of the electric potential surface as discretized into point charges and generated in three rings. Note that each point holds the same number of fundamental charges.

Law [21]. The magnetic field is calculated at each timestep using only the radius and z-position, from the equations shown here:

$$B_r = \frac{\left(\frac{nI\mu_0}{2r_s}\right)\frac{z}{r}}{\pi\sqrt{\left(1+\frac{r}{r_s}\right)^2 + \left(\frac{z}{r_s}\right)^2}} \left\{ E_{el} \frac{1 + \left(\frac{r}{r_s}\right)^2 + \left(\frac{z}{r_s}\right)^2}{\left(1+\frac{r}{r_s}\right)^2 + \left(\frac{z}{r_s}\right)^2 - \left(4\frac{r}{r_s}\right)} - K_{el} \right\} \quad (3.1.5)$$

$$B_z = \frac{\left(\frac{nI\mu_0}{2r_s}\right)}{\pi\sqrt{\left(1+\frac{r}{r_s}\right)^2 + \left(\frac{z}{r_s}\right)^2}} \left\{ E_{el} \frac{1 - \left(\frac{r}{r_s}\right)^2 - \left(\frac{z}{r_s}\right)^2}{\left(1+\frac{r}{r_s}\right)^2 + \left(\frac{z}{r_s}\right)^2 - \left(4\frac{r}{r_s}\right)} + K_{el} \right\} \quad (3.1.6)$$

where E_{el} and K_{el} are the solutions to the elliptical integrals of the first (K) and second (E) kind for the variable m , shown here:

$$m = \frac{4\frac{r}{r_s}}{\left(1+\frac{r}{r_s}\right)^2 + \left(\frac{z}{r_s}\right)^2} \quad (3.1.7)$$

which is calculated by the MATLAB function, `ellipke`. The radial field component is then converted into Cartesian x and y components based on the particle position.

The electric field is calculated by taking the solution for the potential field of a charge monopole, shown here [22]:

$$V = \frac{q}{4\pi\epsilon_0|\vec{r}|} = \frac{q}{4\pi\epsilon_0\sqrt{x^2 + y^2 + z^2}} \quad (3.1.8)$$

Setting the electric field equal to the negative gradient of the potential [22] and showing a single component gives,

$$E_x = -\frac{\partial V}{\partial x} = -\frac{\partial}{\partial x} \left[\frac{q}{4\pi\epsilon_0 \sqrt{x^2 + y^2 + z^2}} \right] \quad (3.1.9)$$

Taking the partial derivative with respect to the single component, x , confers,

$$E_x = \frac{-q}{8\pi\epsilon_0} \frac{2x}{(x^2 + y^2 + z^2)^{3/2}} \quad (3.1.10)$$

Now vector subtraction is added to establish the distance between the monopole and the particle.

$$E_x = \frac{-q}{8\pi\epsilon_0} \frac{2(x - r_x)}{\left[(x - r_x)^2 + (y - r_y)^2 + (z - r_z)^2 \right]^{3/2}} \quad (3.1.11)$$

A discrete summation of positive monopoles is then calculated for all Cartesian direction components at each timestep to solve for the E-field at the particle.

Particle Mover

The particle mover takes input from the electromagnetic field solver and initial condition calculations to set the instantaneous timestep at 0.01 percent of the gyroperiod, defining the resolution of the program. The gyroperiod of a relativistic particle is shown here [5]:

$$\tau_g = \frac{\pi m}{|\vec{B}| q \gamma} \quad (3.1.12)$$

where gamma is the relativistic, or Lorentz, correction shown here [5]:

$$\gamma = \sqrt{1 - \frac{|\vec{v}|^2}{c^2}} \quad (3.1.13)$$

The code then passes the timestep, along with particle velocity and electromagnetic field component values to a 4th order Runge-Kutta integrator to find the new velocity vector. The integrator relies on a formulation of the relativistic Lorentz force shown here:

$$\frac{dv_x}{dt} = \frac{q}{m\gamma} \left[E_x + (v_y B_z - v_z B_y) \right] \quad (3.1.14)$$

$$\frac{dv_y}{dt} = \frac{q}{m\gamma} \left[E_y + (v_z B_x - v_x B_z) \right] \quad (3.1.15)$$

$$\frac{dv_z}{dt} = \frac{q}{m\gamma} \left[E_z + (v_x B_y - v_y B_x) \right] \quad (3.1.16)$$

The new position component is found by simply multiplying the new velocity by the timestep and adding the old position. These positions are stored in a complete position vector for plotting and manipulation by a point of closest approach (POCA) algorithm. The POCA algorithm returns the minimum radius of each particle to the origin, as shown in the results.

3.2 Störmer Region Size Analysis

The approximate area of the Störmer region was evaluated using the data brushing tool within MATLAB R2009b. This allows a user to select individual points of data to extract precise information from a plot. Data was selected first by its proximity to the solenoid radius while still maintaining a smooth transition between points. An example of this is shown in **Figure 22**. Once extracted, the data was run through a Delaunay triangulation function (DelaunayTri in MATLAB R2009b) as shown in **Figure 23** and then a convex hull function (convexHull in MATLAB R2009b). The convex hull function takes the Delaunay triangulation and solves for the edges, then returns the area of the bounded region in the units associated with each axis (in this case, meters by meters). The area between each constant energy case was evaluated for a percent changed. This is done by the equation for standard percent difference, shown here:

$$\left(\frac{A_{new} - A_{old}}{A_{old}} \right) * 100 = PD_{Area} \quad (3.1.17)$$

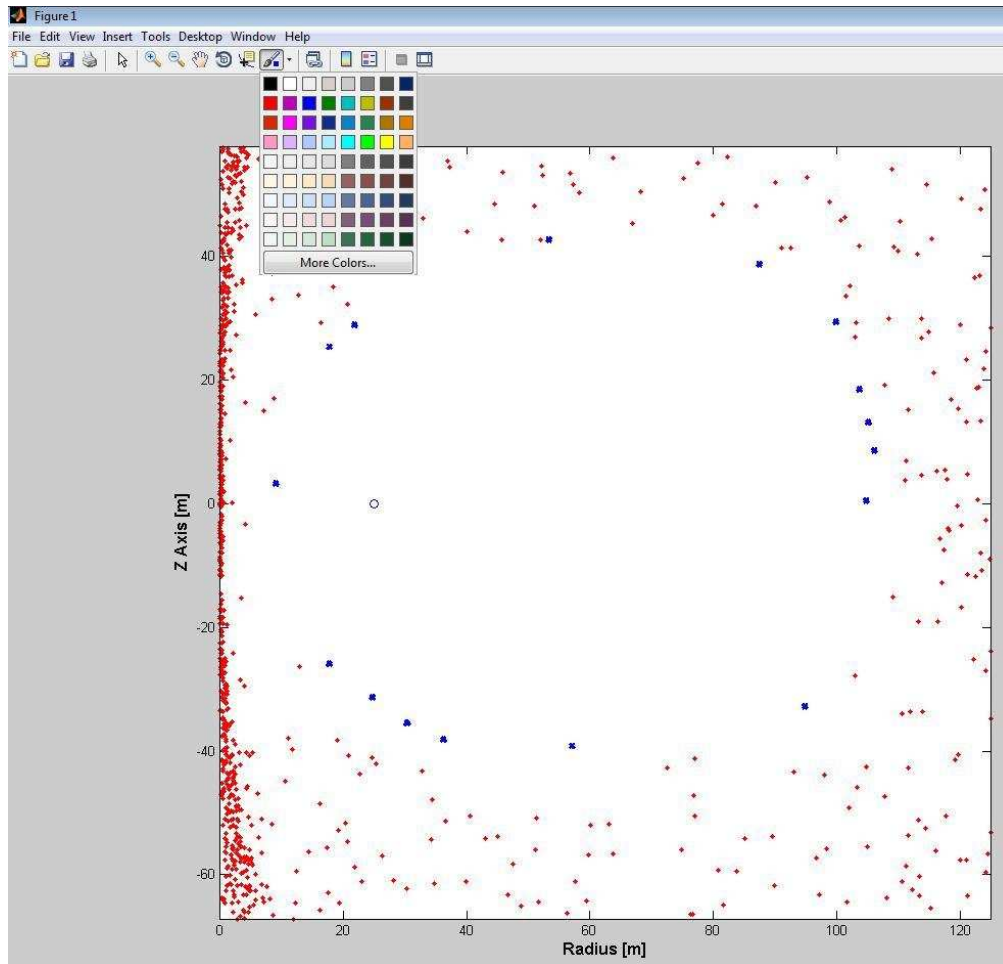


Figure 22: Example showing the selection of points for determining the area of the Störmer region using the data brushing tool in MATLAB R2009b. The selected points are larger dots (blue), with the solenoid radius as a circle (blue) and the non-selected points as regular dots (red).

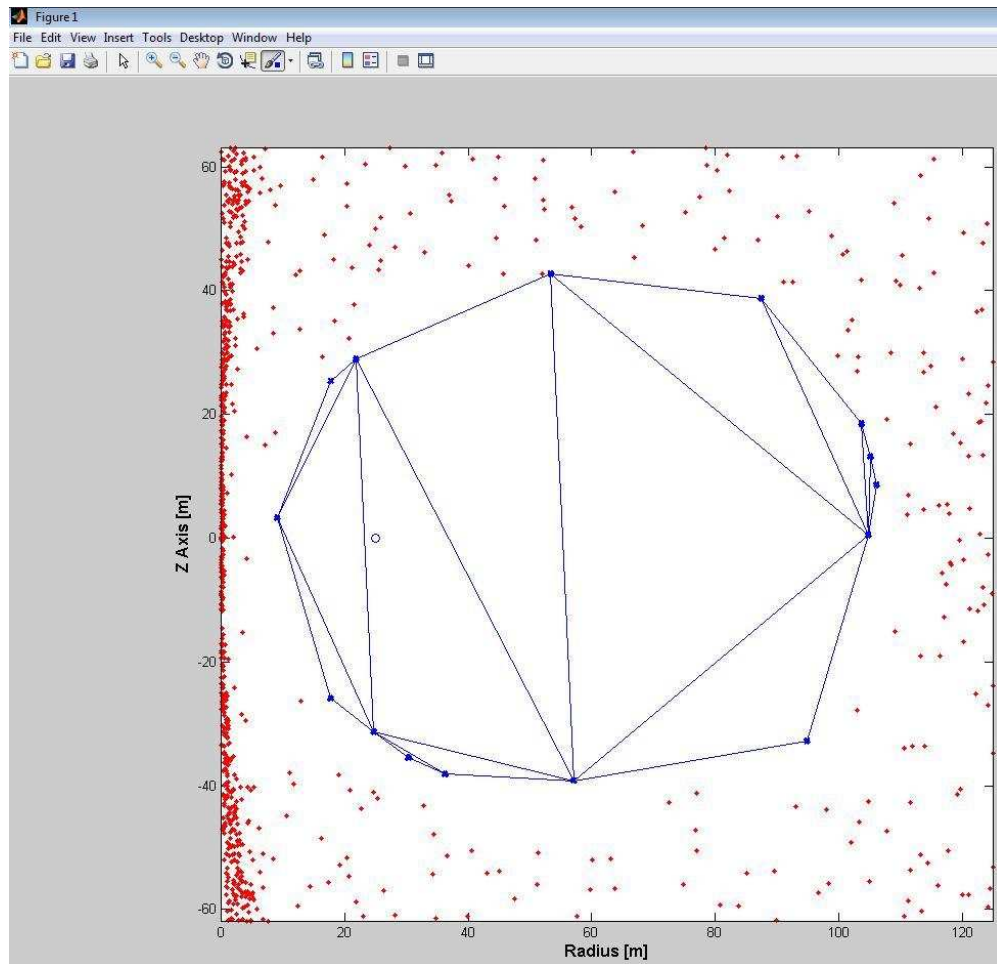


Figure 23: Example showing the creation of the Delaunay triangulation function in MATLAB R2009b. The selected points are larger dots (blue), with the solenoid radius as a circle (blue) and the non-selected points as regular dots (red).

CHAPTER IV

RESULTS AND DISCUSSION

4.1 Code Validation

Particle Mover Validation

Validation of the particle mover was central to validating the code as a whole. Three steps are taken to evaluate the code on a qualitative basis: a simple electromagnetic field test setup, observations of known particle motion phenomena within a magnetic dipole and by comparing with other independent results. The simple test setup involved recording a single particle trajectory through parallel 1D electric and magnetic fields along the positive z-axis, as shown in **Figure 24**. **Figure 25** and **Figure 26** both demonstrate magnetic mirroring at the poles of the solenoid. Note that both the inbound and outbound trajectories are visible and distinct. Comparing the results from Shepherd and Kress [3] in **Figure 27** to **Figure 28**, a good correlation is seen between the results given here and the previous independent results. A small variation in the Störmer region's radial length can be seen, while the z-axis is nearly identical. As a point of validation for both codes, Shepherd and Kress [3] always prescribed to matching the dipole field strength of the solenoid to the average interstellar magnetic field, which resulted in a radius of 50 km. This was done because the ambient interstellar field approximates to the solenoid magnetic field at this length [3]. Also, the difference between electric potential energies for a particle initialized at infinity and 50 km is insignificantly small. Finally, it is unclear what effects the difference in magnetic field calculations from Shepherd and Kress [3] had on the results. The small variation in radial Störmer region length could be the result.

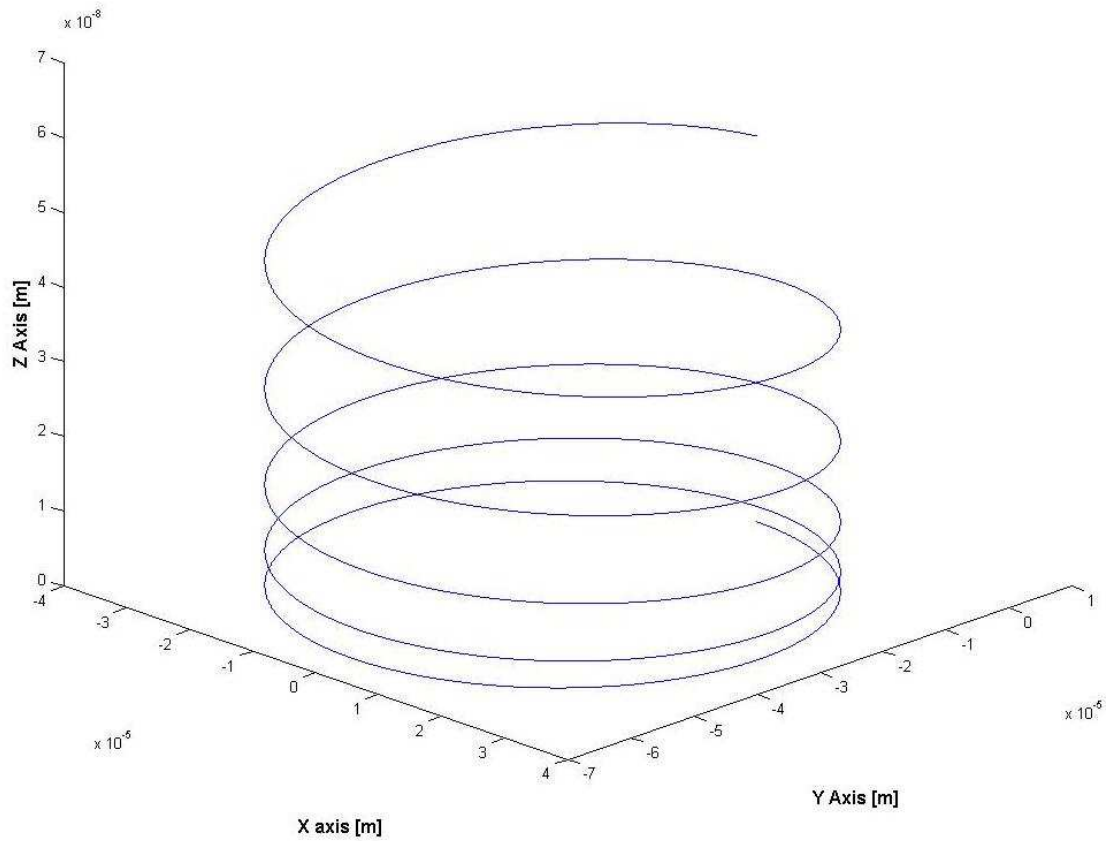


Figure 24: Simple test case for 4th order Runge-Kutta numerical particle mover. Electric and magnetic fields point along the positive z-axis. Note the widening between spirals due to electric potential acceleration.

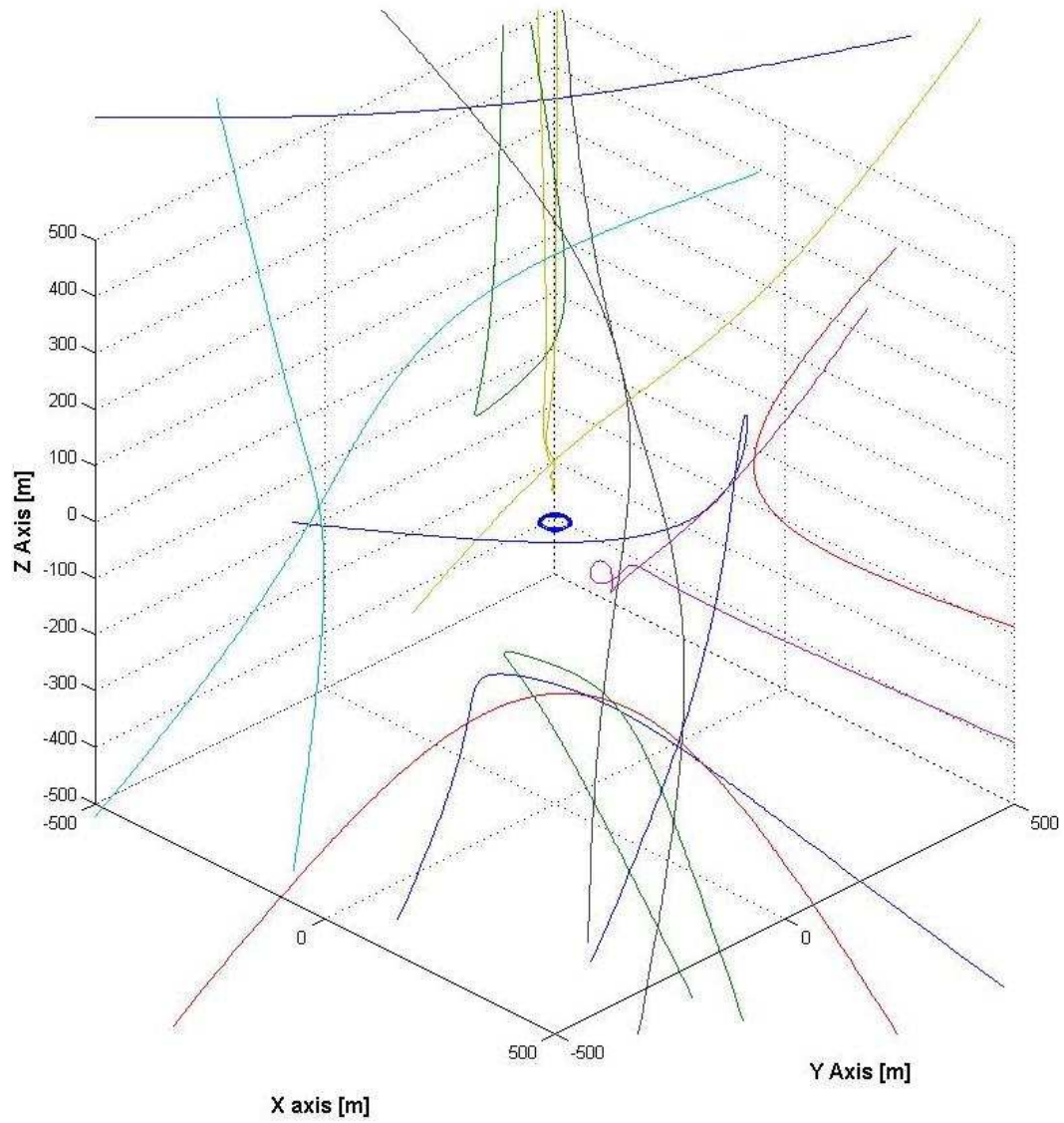


Figure 25: 3D plot of 1 GeV iron ion trajectories within a magnetic dipole of moment $1.1 \times 10^{13} \text{ A m}^2$. Note the magnetic mirroring at the poles of the solenoid.

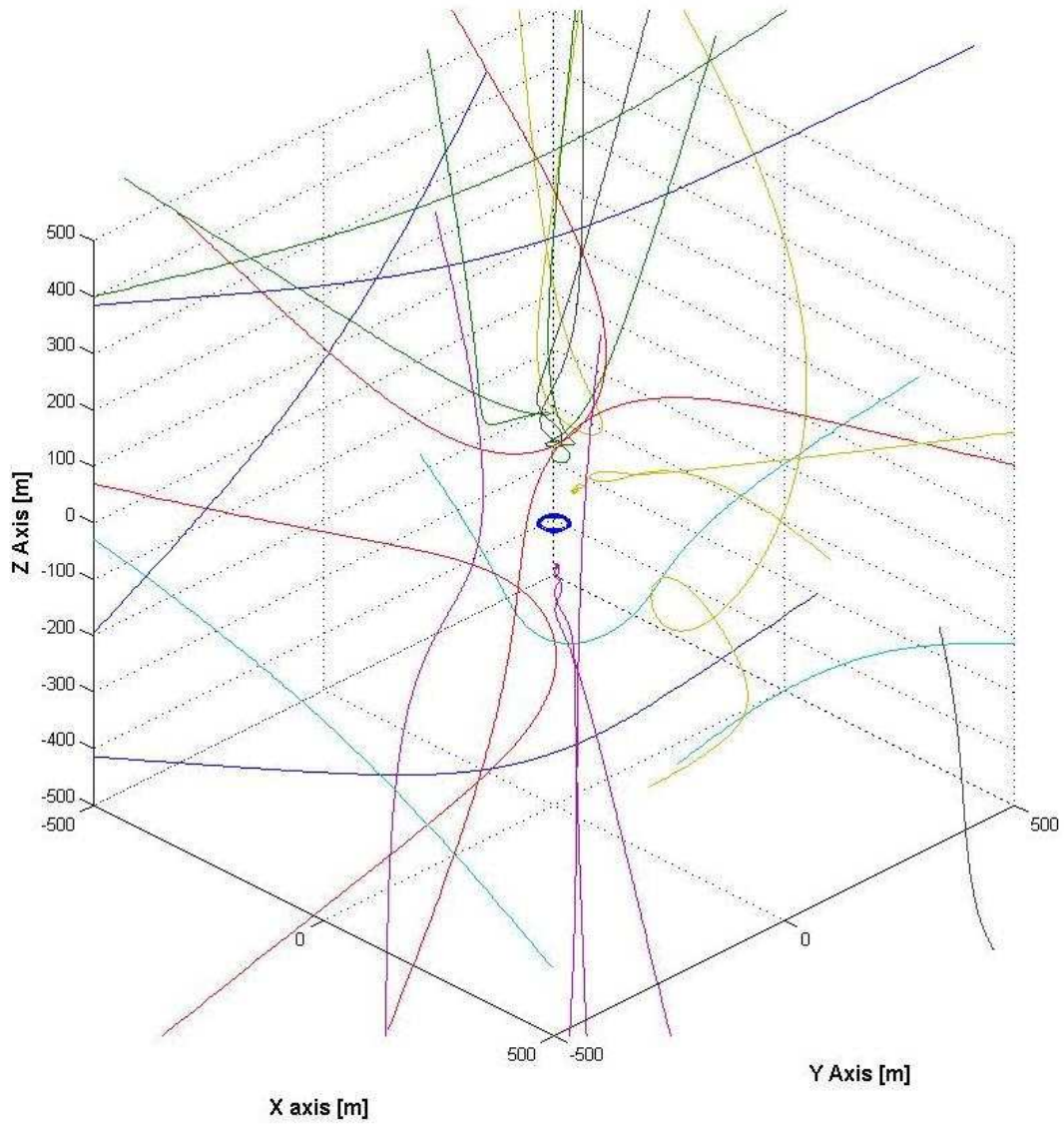


Figure 26: Additional 3D plot of 1 GeV iron ion trajectories within a magnetic dipole of moment $1.1 \times 10^{13} \text{ A m}^2$ and a 20 MV positive electrostatic potential.

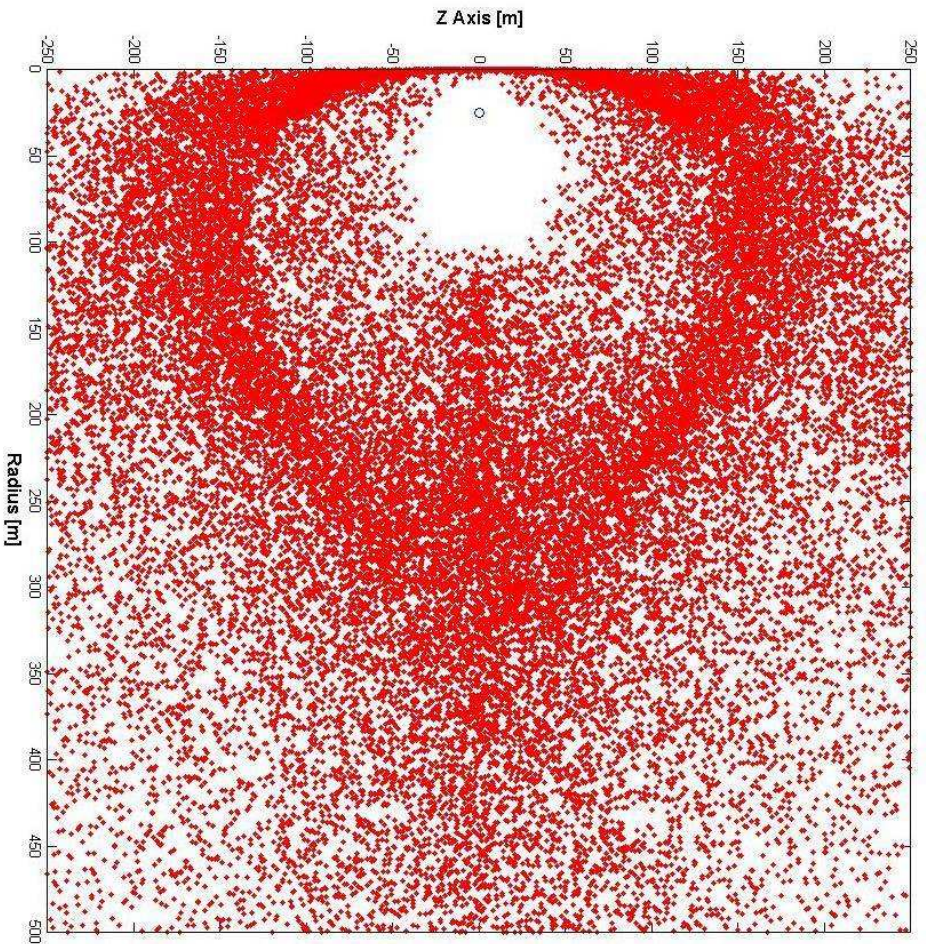


Figure 27: 50,000 iron ions (red dot) simulated at 1 GeV with a solenoid (blue circle) magnetic moment of $1.1 \times 10^{13} \text{ A m}^2$

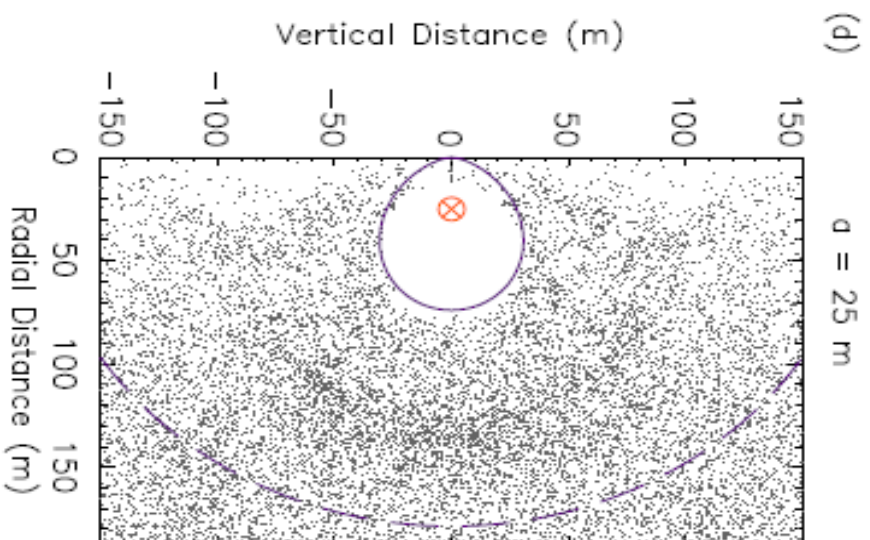


Figure 28: Results from [3] with grey dots representing particles with the solenoid as a red crossed circle. Note the dimensions of the tallest and widest points within the Störmer region for comparison.

Particle Count Validation

The validation of random seed numerical codes is often difficult due to the difficulty in quantifying outcomes, but it can show comparable qualities. In order to properly capture the main qualities (all possible particle trajectories), large numbers of simulated particles are required. This, however, proved to be prohibitively processor intensive, forcing simulations to run for a collective 16 hours calculating 5×10^4 particle trajectories. Because of the long computation time only two results were obtained using this large sampling group, with all following simulations run at 2×10^4 . This proved to be a good sample size to clearly define the Störmer region, as variations between **Figure 27** and **Figure 29** are visually insignificant.

Electric Field Summation Validation

The toroidal charge summation (Eqs. 3.1.10 & 3.1.11) is valid on two bases. First, according to Gauss's Law, the electric field gradient is directly proportional to the total charge density. Because this is a linear relation, the superposition principle is valid then for any charge density. This verifies that the discrete summation of clustered charges accurately describes an electric field, through the superposition principle. Therefore, the second issue comes from correctly distributing the charge in the simulated three-dimensional space. The torus surface is at a 20 MV potential to its surrounding space (including spacecraft), not an adjacent plate. Therefore, an assumption using two parallel plates was invalid. In order to properly capture the assumed capacitance, a hollow conducting sphere at an identical radius to the torus was referenced to infinity and set as the torus's capacitance.

4.2 Results

Plots detailing the radial and vertical points of closest approach to the origin were generated based on varying particle energy and electromagnetic field strengths. This was done for specific comparison to the work by Shepherd and Kress [3], but also clearly shows variations in the Störmer region between plots with electric potentials present. Note that all results contain 2×10^4 particles at a 1.1×10^{13} A m² magnetic dipole moment. **Figure 29** and **Figure 30** correspond to r-z plots at a 1 GeV particle energy, but **Figure 30** also presents a 20 MV potential. Note the variation in the Störmer region near the origin in **Figure 30**. Decreasing the particle energy, **Figure 31** and **Figure 32** correspond to r-z plots at a 150 MeV particle energy, while **Figure 32** also presents a 20 MV potential. Note the shape of the Störmer region in **Figure 32**, with pointed lobes generated above and below the solenoid radius and a slight increase in radial length. Decreasing particle energy further, and **Figure 34** correspond to r-z plots at a 100 MeV particle energy, while **Figure 34** also presents a 20 MV potential. Note the shape of the Störmer region in **Figure 34**, with more well defined vertical lobes than **Figure 32** and a visible overall size increase. The Störmer region of each plot, quantified as an approximate area, is found in **Table 2**. **Figure 35** shows these results as the percent area increased versus ratio of particle energy (electron-Volts) per electrostatic shield potential (Volts). Note that this ratio is in units of elementary charge, a constant.

4.3 Discussion

Evaluating the effects of an electric potential proved to be less conclusive at particle energies orders of magnitude above the shielding potential. Because the electron-Volt is a standard unit of energy gained by an electron accelerating through one Volt of negative electric potential (direction of proton flow is

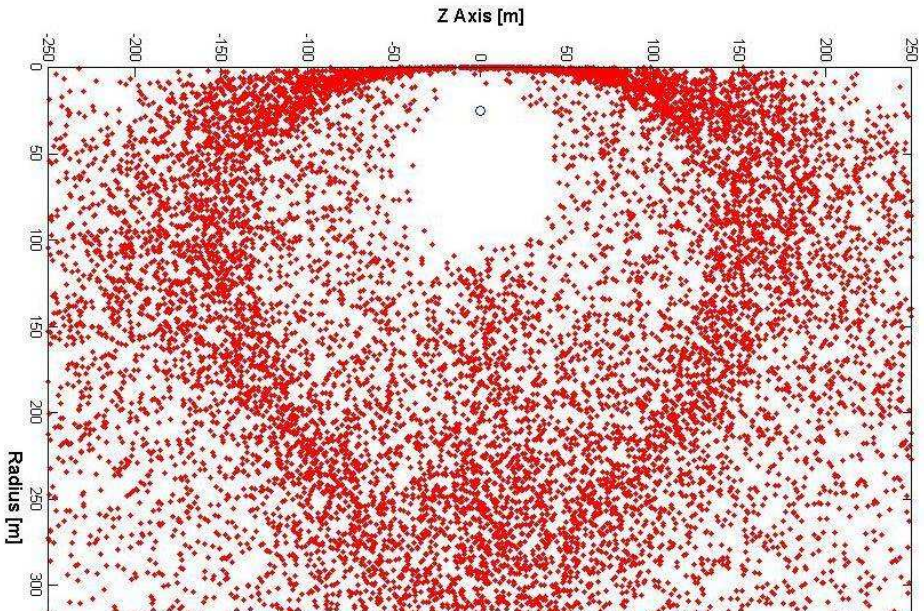


Figure 29: 20,000 iron ions (red dot) simulated at 1 GeV with a solenoid (blue circle) magnetic moment of $1.1 \times 10^{13} \text{ A m}^2$.

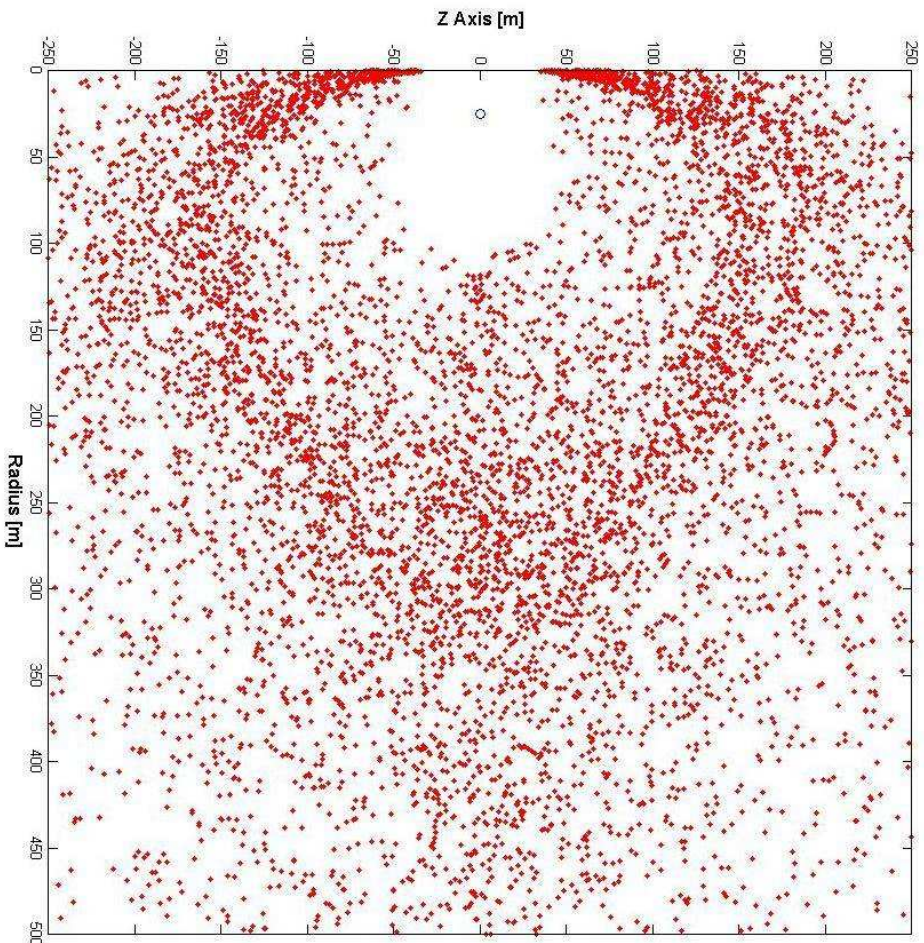


Figure 30: 20,000 iron ions (red dot) simulated at 1 GeV with a solenoid (blue circle) magnetic moment of $1.1 \times 10^{13} \text{ A m}^2$ and a 20 MV electric potential. Note the gap generated at the origin.

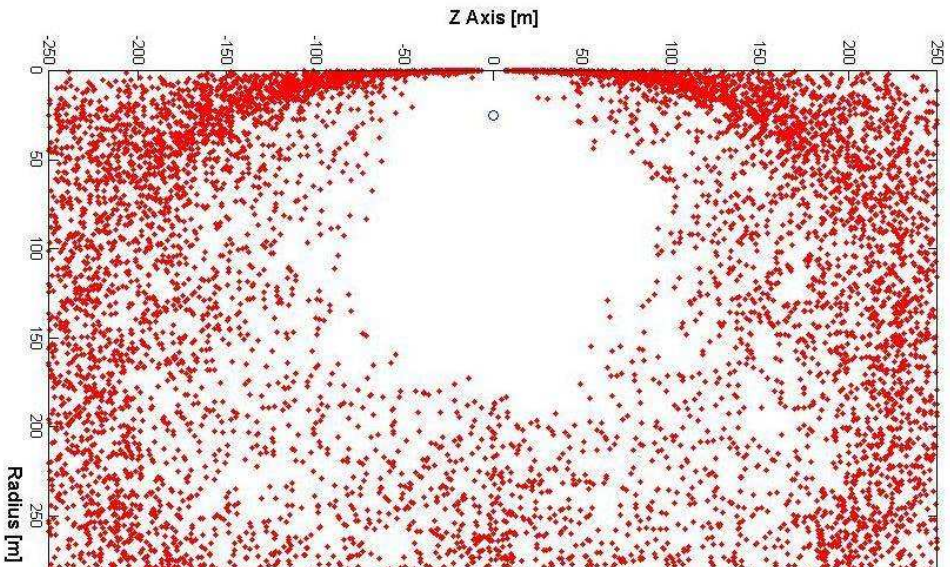


Figure 31: 20,000 iron ions (red dot) simulated at 150 MeV with a solenoid (blue circle) magnetic moment of $1.1 \times 10^{13} \text{ A m}^2$.

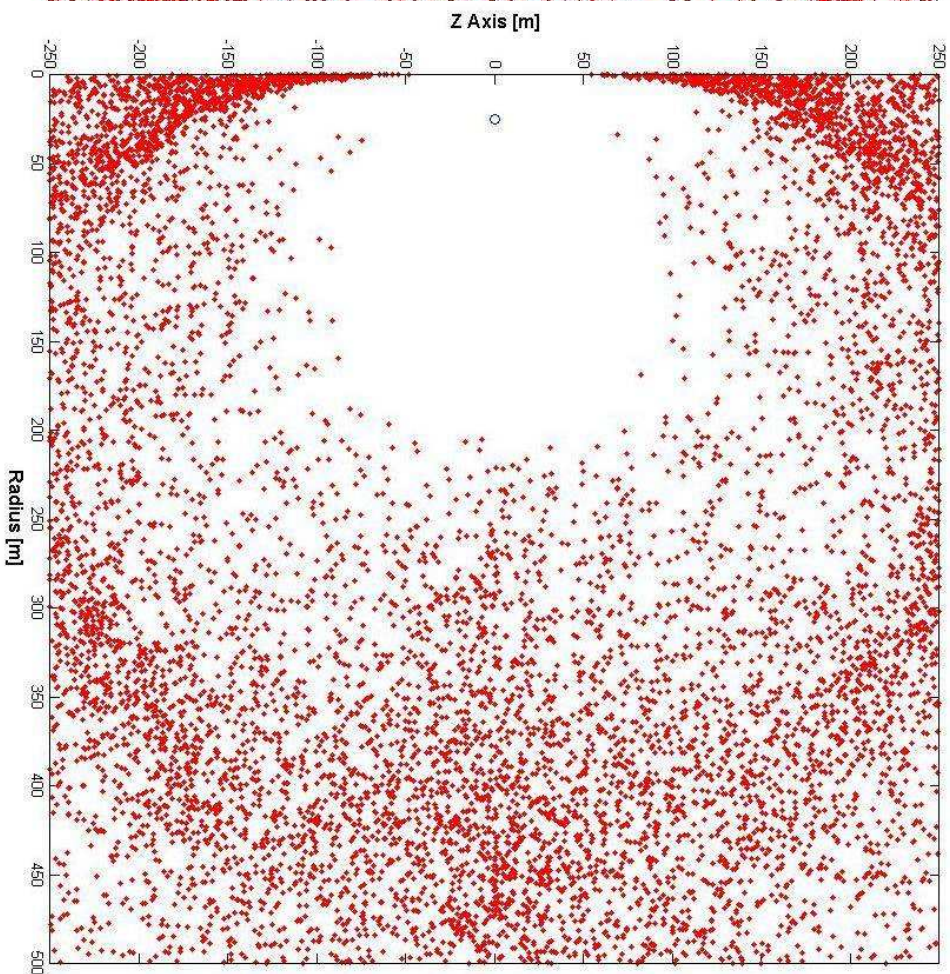


Figure 32: 20,000 iron ions (red dot) simulated at 150 MeV with a solenoid (blue circle) magnetic moment of $1.1 \times 10^{13} \text{ A m}^2$ and a 20 MV electric potential. Note the gap generated at the origin, with increased Störmer region size directly above and below the solenoid and along the radial length.

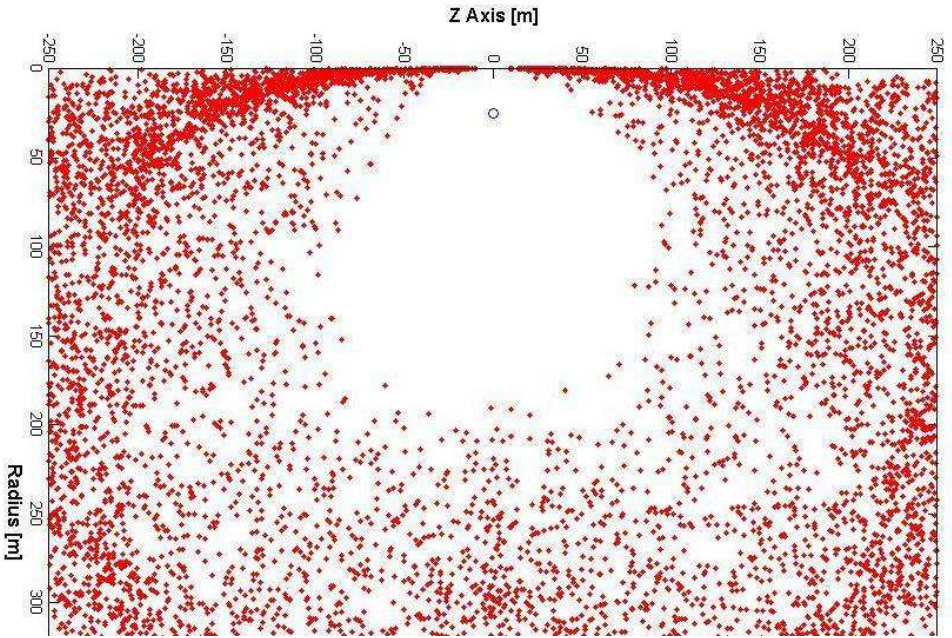


Figure 33: 20,000 iron ions (red dot) simulated at 100 MeV with a solenoid (blue circle) magnetic moment of $1.1 \times 10^{13} \text{ A m}^2$

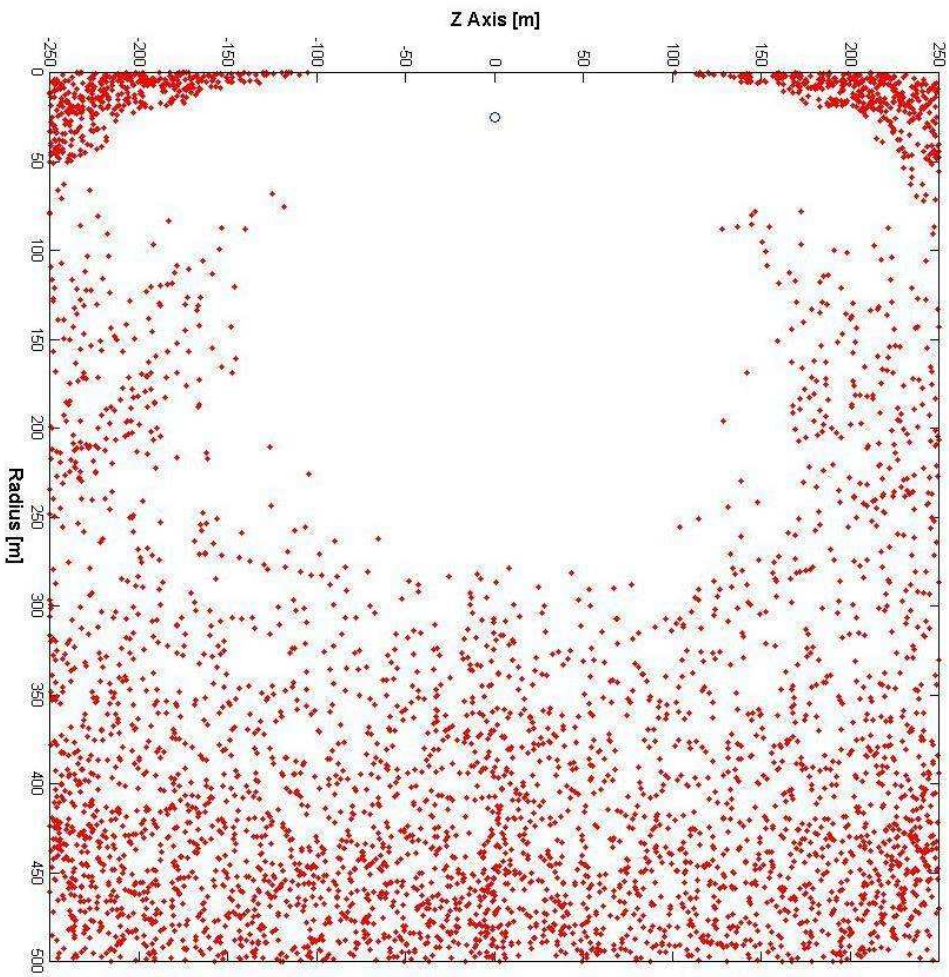


Figure 34: 20,000 iron ions (red dot) simulated at 100 MeV with a solenoid (blue circle) magnetic moment of $1.1 \times 10^{13} \text{ A m}^2$ and a 20 MV electric potential. Note the very similar shape of the Störmer region as compared to Figure 32, with increased scale.

Table 2: Results of Störmer area analysis from r-z plots

Particle Energy [eV]	Particle Energy/ Electrostatic Potential [e]	Area (No E-Potential) [m ²]	Area (E-Potential) [m ²]	Area Increase [%]
1.00E+08	5.0E+00	2.39E+04	7.27E+04	204.44%
1.50E+08	7.5E+00	1.83E+04	3.38E+04	84.56%
1.00E+09	5.0E+01	6.27E+03	7.98E+03	27.26%

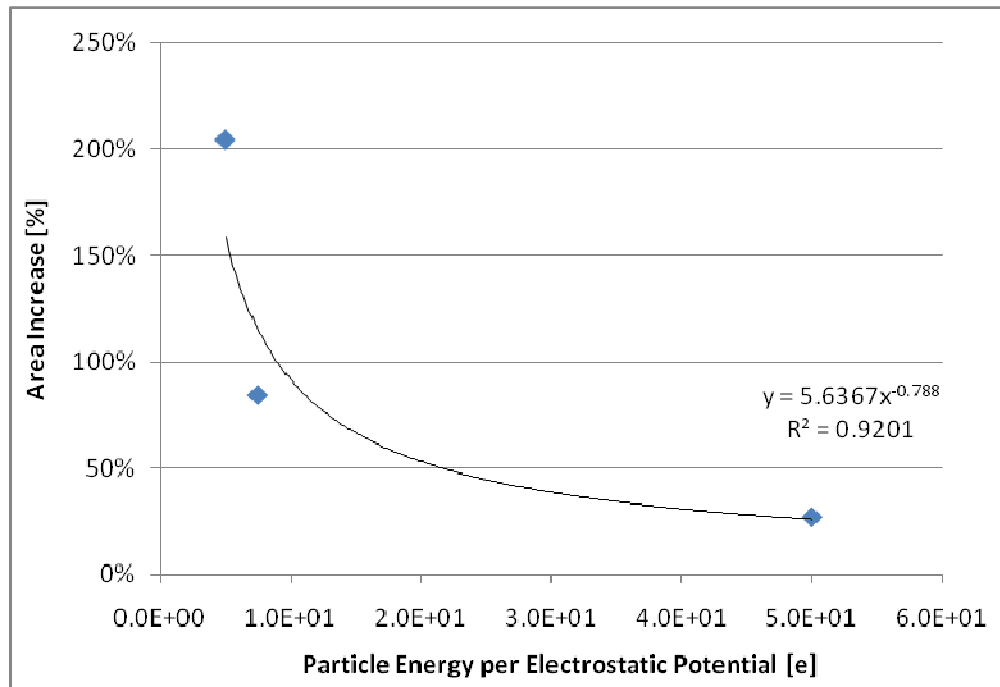


Figure 35: Percent area increase as a function of the ratio between the particle energy and electrostatic potential.

considered positive), the opposite is true for deceleration. This would be the energy lost by the electron as it approached a positive potential. At a 20 MV potential, the electrical shield should repel any positively charged particle at or below 20 MeV. Any particle with higher energy could be deflected but not completely reversed if the incident vector was aimed directly at the shield (assuming no magnetic field effects). With the included magnetic dipole field, the time a particle takes to approach the electric shield increases due to the induced curvature. This should further decelerate high energy particles, which directly translates into a larger Störmer region (refer to equation 1.2.13).

Main observations

Now, examining the differences between **Figure 29** and **Figure 30**, **Figure 31** and **Figure 32**, and **Figure 33** and **Figure 34**, it is clear that the electric shield has a proportional effect on the Störmer region. The variations between **Figure 29** and **Figure 30** are the least distinct, largely due to the high particle energy. The iron ions carry fifty times the energy necessary to penetrate the electric shield alone, so it is reasonable to expect that these plots are the least affected. However, the main difference is located around the origin in. This is from the greater energy loss of particles magnetically mirroring at the poles than those near the magnetic equator. Ions in this trajectory spend more time at close proximities to the electric shield surface, which translates into a larger total energy change. **Figure 32** and **Figure 34** also illustrate this, albeit with increased scale. Another phenomenon generated by the electric potential was the creation of excluded lobes along a vertical axis from the torus radius. This is most likely due to the geometrical setup, as the electric charge distribution was located at this radius. Finally, the overall size of the excluded region increased at larger radii from the torus in each case, with more sizeable increases the smaller the ratio of particle energy to electrostatic shield potential. This is shown more clearly in **Figure 35**. Because of a lack of data, overall error analysis is unavailable. If random error could be analyzed, the quantification of the Störmer

region area has two sources of random error: sparse data points along the edge and human error in selecting actual boundary points. Selection of the Störmer region boundary was done by a human, but that does not necessarily indicate a significant human error. The points along the assumed edge of the excluded area were sparse enough that minimal evaluation was needed to determine points along the boundary. The error is most likely found in the sparse nature of the plots. Without a large number of particles along the region boundary, the interpolated edge is not smooth. This would present a small amount of error without any ability for analytical comparison. Therefore in order to properly define the overall error, the experiment needs to be repeated with the same user for each case.

General comments

Initially, representing data with plots of a particle's point of closest approach was a cause of concern because it does not guarantee that particles are excluded from the Störmer region. Shepherd and Kress [3] dealt with this by showing a 3D plot of particle trajectories colored to signify their proximity to the origin, as shown in **Figure 36**. A better method would model the predicted Störmer region as a surface volume and capture the surface particle flux.

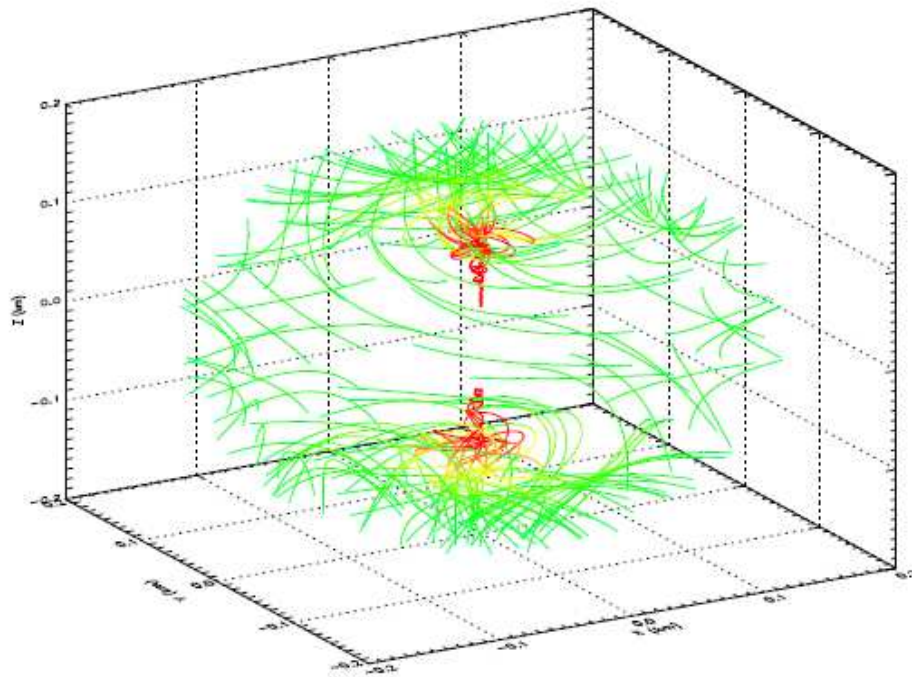


Figure 36: 3D plot of particle trajectories colored to indicate proximity to origin (red is closer, green farther). Note that this demonstrates the validity of the Störmer region r - z plots because no particles pass through the region before their point of closest approach is recorded [3].

CHAPTER V

CONCLUSION

A basic hybrid radiation shield concept was predicted to provide a more effective method of shielding a habitable torus region than a solenoid acting alone. A numerical experiment was performed to evaluate this statement. It was shown that the electrostatic potential influences the size of the Störmer dipole exclusion region, and the ratio of particle energy to electrostatic potential is significant in determining the amount increased. A decrease in the particle energy per electrostatic potential ratio from 50 to 5 gives an order of magnitude increase in the exclusion area percent difference, from 27% to 204%.

Future work is needed to define this relationship to an acceptable level of certainty. First, duplication of this experiment is needed to provide more data, enabling the total error associated with these results to be found. Also, electrostatic potential effects on the lighter particle spectra found in the interstellar plasma for both positive and negative charges must be examined (i.e., electrons, protons, oxygen ions, etc.). Development of a relation that modifies Störmer's dipole exclusion region solution would allow us to move towards a more complete analytical model. This would account for a current carrying solenoid at some real radius with an added electric potential (likely due to a spherical potential body) to define the actual size and shape of the excluded region, analogous to Störmer's results for the ideal magnetic dipole. Finally, a positive comparison to experimental results would solidify both components.

LIST OF REFERENCES

LIST OF REFERENCES

1. Parker, E. N., Shielding space travelers, *Sci. Amer.*, 294, 40.47, 2006.
2. Buhler, Charles R., "Analysis of a Lunar Base Electrostatic Radiation Shield Concept", NIAC CP 04-01 Phase I, Final Report, April 28, 2005.
3. Shepherd, S.G. and Kress, B.T., "Störmer Theory Applied to Magnetic Spacecraft Shielding" *Space Weather*, 4, 2007.
4. Störmer, C., *The Polar Aurora*, Oxford Univ. Press, 1955.
5. Gombosi, Tamas I., *Physics of the Space Environment*, Cambridge Univ. Press, 1998.
6. Cougnet, C. *et al.*, "Radiation Exposure and Mission Strategies for Interplanetary Manned Missions (REMSIM)", Springer, May 2005.
7. Lobascio C., Cougnet C., Guarnieri V., Guatelli S., Pia M. G., Rampini R., and Tracino E.: 2004a, "Review and Analysis of Existing Vehicle Concepts", (REMSIM Technical Note 2), Alenia Spazio Technical Note.
8. Watkins, S.A., "Magnetic Shielding of Spacecraft Employing High-Temperature Superconductors", Thesis, Duke University, 1993.
9. Parker, E. N., "Shielding space explorers from cosmic rays", *Space Weather*, 3, 2005.
10. Sussingham, J. C., Watkins, S. A., and Cocks, F. H., "Forty years of development of active systems for radiation protection of spacecraft", *J. Astronautical Sci.*, 47, 165.175, 1999.
11. Buhler, Charles R., "Analysis of a Lunar Base Electrostatic Radiation Shield Concept", NIAC CP 04-01 Phase I, Progress Report #2, February 15, 2004.
12. Dupont, Dupont Films; "Corona Resistant Kapton CR Takes Electrical Insulation Design and Reliability to New Levels", H-54505-1, http://www2.dupont.com/Kapton/en_US/assets/downloads/pdf/CR_H-54506-1.pdf, retrieved July 16, 2010.

13. World Health Organization, "Environmental Health Criteria 232: Static Fields" WHO Press, 2006.
14. Slough, J., "The Plasma Magnet", NIAC Phase I Final Report, University of Washington
15. Townsend, L.W., "Overview of active methods for shielding spacecraft from energetic space radiation", *11th Annual NASA Space Radiation Health Investigators' Workshop*, Arona, Italy, 2000.
16. Cocks, J. C., Watkins, S. A., Cocks, F. H., and Sussingham, C., "Applications for deployed high temperature superconducting coils in spacecraft engineering: A review and analysis", *J. British. Interplanetary Soc.*, 50, 479-484, 1997.
17. Dilão, R. and Alves-Pires, R., "Chaos in the Störmer Problem", arXiv:0704.3250v1 [nlin.CD], 24 Apr 2007
18. Schuster, H.G., *Deterministic Chaos: An Introduction*, 3rd augm. ed., Weiheim, VCH, 1995
19. Matsumoto, M. and Nishimura, T., "Mersenne Twister: A 623-Dimensionally Equidistributed Uniform Pseudorandom Number Generator", *ACM Transactions on and Computer Simulations: Special Issue on Uniform Random Number Generation*, 1998.
20. Hecht, Eugene, *Physics: Calculus*, Cengage Learning, 2000.
21. Montgomery, D. Bruce, and Terrell, J., "Some Useful Information for the Design of Air-core Solenoids", Air Force Contract AF19(604)-7344, November, 1961.
22. Jackson, John David, *Classical Electrodynamics*, 3rd. ed., John Wiley & Sons Inc., 1999.
23. Wilson, John W. 1978: Environmental Geophysics and SPS Shielding. *Workshop on the Radiation Environment of the Satellite Power System*, Walter Schimmerling and Stanley B. Curtis, eds., LBL-8581 (Contract W-7405-ENG-48), Univ. of California, Sept. 15, pp. 33-116.

24. Fisk, L. A., "Solar modulation of galactic cosmic rays," in *Solar Terrestrial Physics*, R. L. Carovillano and J. M. Forbes, eds., p. 217, D. Reidel, Dordrecht, The Netherlands, 1983.
25. Schwadron, N. A., Fisk, L. A., and Gloeckler, G., "Statistical acceleration of interstellar pickup ions in corotating interaction regions," *J. Geophys. Res.*, 23, 2871-2874, 1996.
26. Parker, James F., Jr.; and West, Vita R., eds. 1973: *Bio-astronautics Data Book*, Second ed. NASA SP-3006.
27. Bernert, R.E., and Stekly, Z.J.J., "Magnetic Radiation Shielding Systems Analysis", AVCO-Everett Research Laboratory, July 1964.
28. Hoffman, J.A., Fisher, P. and Batischev, O., "Use of Superconducting Magnet Technology for Astronaut Radiation Protection", NIAC Phase I Final Report, Contract CP 04-01, May 2, 2005.
29. National Bureau of Standards, Circular Number 74, *Radio instruments and Measurements*, 2nd Edition, Washington, DC (1924), p.250.

APPENDIX

Appendix A: Figures and Tables

Table 3: Average solar wind properties at 1 AU [5].

Quantity	Value	Units
Electron concentration	7.1	cm^{-3}
Flow speed	450	km/s
Proton temperature	1.2×10^5	K
Electron temperature	1.4×10^5	K
Magnetic field	7.0	nT
Acoustic speed	60	km/s
Alfvén speed	40	km/s
Average collision time	3.5×10^6	s
Travel time to 1 AU	3.5×10^5	s

Table 4: Heliospheric parameters at 1 AU [5].

Quantity	Symbol	Value	Units (SI)
Astronomical Unit	AU	1.496×10^{11}	m
Equatorial solar wind	mean density	n	8.7 cm^{-3}
	mean speed	u	470 km s^{-1}
	particle flux	nu	$3.8 \times 10^8 \text{ cm}^{-2} \text{ s}^{-1}$
	α particle abundance	A_α	%
	proton temperature	T_p	$1.2 \times 10^5 \text{ K}$
	electron temperature	T_e	$1.4 \times 10^5 \text{ K}$
	α temperature	T_α	$5.8 \times 10^5 \text{ K}$
	mean magnetic field	B	6.2 nT
Polar solar wind	mean density	n	2.5 cm^{-3}
	mean speed	u	770 km s^{-1}
	mean magnetic field	B	2.5 nT
	particle flux	nu	$1.9 \times 10^8 \text{ cm}^{-2} \text{ s}^{-1}$

Appendix B: Source Code

```
%% Particle Transport Code using both electric potential and magnetic field
% Finding the point of closest approach to the origin
% Author: Benjamin Klamm
tic%%%%%%%%%%%%%%%%%%%%%%%%%%%%%%%%%%%%%%%% Time
%%%%%%%%%%%%%%%%%%%%%%%%%%%%%%%%%%%%%%%%
close('all')
clear
clc
pause off

%% Fundamental Constants
% Fundamental Charge [Coulomb]
q = 1.6022E-19;
% Speed of light [m/s]
c = 299792458;
% Permeability of Free Space
Mu0 = (4*pi)*(10^-7);
% Permittivity of Free Space
Epsilon0 = 8.8542E-12;
% Electron Mass [kg]
MassE = 9.1094E-31;
% Proton/Neutron Mass [kg]
MassP = 1.67262E-27;
MassN = 1.67493E-27;

%% User Defined Constants
nd = 20; % number of dipoles in torus approximation
nt = 175; % number of turns for the solenoid
I = 3.2E7; % Current [Amp]
Vpot = 20E6; % Voltage potential across dipole torus [V]
rloop = 25; % rloop is the solenoid loop radius [m]
torR = 1.75; % torus radius [m]
tsa = 4*(pi()^2)*rloop*torR*(.85); % Torus surface area approximation
% for E-Shield [m^2]
d = 1; % distance between E-Potential dipoles [m]
qo = ((4*pi*Epsilon0*Vpot*tsa)/(d*nd*3))*(6.241509E18); % qo is the
% number
% of elementary charges for each of the
% discrete dipoles in the E-potential
qp = 1; % qp is the sign of the charge (positive, negative)
nq = 1; % nq is the number of charges (doubly ionized, singly ionized,
% fully ionized, etc.)
mp = (26*MassP) + (30*MassN) + (0*MassE); % mp is the total particle
% mass [kg]
k = 100000; % k is the number of initialized values for the
% position matrices
res = 0.001; % resolution as a percent of the gyroperiod
% determined by the timestep (i.e.- %1 equals 100 points
% along the gyroradius)
```

```

numpart = 20000; % number of simulated particles
dist = 50000; % particle initializing distance [m]
random = rand(3,numpart); % 3 random numbers for each particle
                        % generated by Mersenne Twister Alg.
Ep = (150E6-59.537E6)*(1.60217646E-19); % particle kinetic energy input
                        % in eV [J] (50km to 1km = -59.537E6 eV)
vmag = ((c^2)-(c^2/((Ep/(mp*(c^2)))+1)))^(1/2); % particle velocity
                        % magnitude [m/s]
Gamma = (1-((vmag^2)/(c^2)))^(1/2); % Relative motion correction
Bnot = (nt*I*Mu0)/(2*rloop); % Magnetic field strength at
                        % origin of solenoid

```

```

%% Particle Mover

```

```

% initialize matrices
r1 = zeros(nd,3); %
r3 = zeros(nd,3); % position matrices for the torus
r5 = zeros(nd,3); %

endpos = zeros(k,3); % output position matrix
clap = zeros(numpart,2); % point of closest approach to origin on r-z
                        % plane
posmag = zeros(k,1); % magnitude of all position vectors

% Generates n number electric dipoles in an annulus
% radius of loop, rloop, distance between poles, d, and number of
% dipoles, n.
% returns inner ring, r1, and outer ring, r2

```

```

for j=1:nd
    % ring 1 position vector
    r1(j,1) = rloop*cos(j*((2*pi)/nd));
    r1(j,2) = rloop*sin(j*((2*pi)/nd));
    r1(j,3) = 0;
    % ring 2 position vector
    r3(j,1) = (rloop-torR)*cos(j*((2*pi)/nd));
    r3(j,2) = (rloop-torR)*sin(j*((2*pi)/nd));
    r3(j,3) = torR;
    % ring 3 position vector
    r5(j,1) = (rloop-torR)*cos(j*((2*pi)/nd));
    r5(j,2) = (rloop-torR)*sin(j*((2*pi)/nd));
    r5(j,3) = -torR;
end

```

```

% Main Loop
for h=1:numpart
    h
    % Initial conditions
    % position [m]
    xo = dist*sin(2*pi*random(1,numpart+1-h))*...
        cos(pi*random(2,numpart+1-h)); % uses random number starting
    yo = dist*sin(2*pi*random(1,numpart+1-h))*...

```

```

sin(pi*random(2,numpart+1-h));% from end for a set radius
zo = dist*cos(2*pi*random(1,numpart+1-h));% of dist meters
% magnitude of random numbers for unit vector calculation
randmag = ((random(1,h)^2)+(random(2,h)^2)+(random(3,h)^2))^(1/2);
% velocity vector components [m/s]
vox = (-xo/dist)*vmag*(random(1,h)/randmag);%
voy = (-yo/dist)*vmag*(random(2,h)/randmag);% uses random numbers
voz = (-zo/dist)*vmag*(random(3,h)/randmag);% starting from front
for i=1:k
    if (((xo^2)+(yo^2)+(zo^2))^(1/2)) < (dist + 1)
        % Aggregate constant
        Alpha = (qp*q*nq)/(Gamma*mp);

        %% find new electromagnetic fields

        % B-field due to a current carrying wire loop (solenoid)
        % This function finds the magnetic dipole field vector
        % components, Br & Bz, for a solenoid at any point (r,z)
        % for radius of loop, rloop, current, I, and # turns, nt

        r = ((xo^2)+(yo^2))^(1/2);

        Q = ((1+(r/rloop))^2)+((zo/rloop)^2);

        m = (4*(r/rloop))/Q;
        [K,E] = ellipke(m);

        Br = ((Bnot*(zo/r))/(pi*Q^(1/2)))*((E*((1+(r/rloop)^2)+...
            ((zo/rloop)^2))/(Q-(4*(r/rloop)))))-K);
        Bz = ((Bnot)/(pi*Q^(1/2)))*((E*((1-(r/rloop)^2)-...
            ((zo/rloop)^2))/(Q-(4*(r/rloop)))))+K);

        % E-field due to an n number discrete E-dipole annulus
        % qo is the discretized surface charge on the negative
        % surface NOTE: Dipoles are assumed to be always pointing
        % radially out from z=0

        % Initialize E-field to zero
        Ex = 0;
        Ey = 0;
        Ez = 0;

        % Calculate E-field for any point in space
        j=1;
        for j=1:nd
            % Electric Field components
            ExC1 = ((q*qo)/(Epsilon0*4*pi))*(((xo-r1(j,1))/...
                (((xo-r1(j,1))^2)+(yo-r1(j,2))^2)+...
                ((zo-r1(j,3))^2))^(3/2)));
            EyC1 = ((q*qo)/(Epsilon0*4*pi))*(((yo-r1(j,2))/...
                (((xo-r1(j,1))^2)+(yo-r1(j,2))^2)+...
                ((zo-r1(j,3))^2))^(3/2)));

```

```

EzC1 = ((q*qo)/(Epsilon0*4*pi))*(((zo-r1(j,3))/...
    (((xo-r1(j,1))^2)+((yo-r1(j,2))^2)+...
    ((zo-r1(j,3))^2))^(3/2)));
ExC3 = ((q*qo)/(Epsilon0*4*pi))*(((xo-r3(j,1))/...
    (((xo-r3(j,1))^2)+((yo-r3(j,2))^2)+...
    ((zo-r3(j,3))^2))^(3/2)));
EyC3 = ((q*qo)/(Epsilon0*4*pi))*(((yo-r3(j,2))/...
    (((xo-r3(j,1))^2)+((yo-r3(j,2))^2)+...
    ((zo-r3(j,3))^2))^(3/2)));
EzC3 = ((q*qo)/(Epsilon0*4*pi))*(((zo-r3(j,3))/...
    (((xo-r3(j,1))^2)+((yo-r3(j,2))^2)+...
    ((zo-r3(j,3))^2))^(3/2)));
ExC5 = ((q*qo)/(Epsilon0*4*pi))*(((xo-r5(j,1))/...
    (((xo-r5(j,1))^2)+((yo-r5(j,2))^2)+...
    ((zo-r5(j,3))^2))^(3/2)));
EyC5 = ((q*qo)/(Epsilon0*4*pi))*(((yo-r5(j,2))/...
    (((xo-r5(j,1))^2)+((yo-r5(j,2))^2)+...
    ((zo-r5(j,3))^2))^(3/2)));
EzC5 = ((q*qo)/(Epsilon0*4*pi))*(((zo-r5(j,3))/...
    (((xo-r5(j,1))^2)+((yo-r5(j,2))^2)+...
    ((zo-r5(j,3))^2))^(3/2)));
% E-field Summation
Ex = Ex + ExC1 + ExC3 + ExC5;
Ey = Ey + EyC1 + EyC3 + EyC5;
Ez = Ez + EzC1 + EzC3 + EzC5;
end
%% Move Particle
Bmag = ((Br^2)+(Bz^2))^(1/2); % Magnetic Field Strength [T]
r = ((xo^2)+(yo^2))^(1/2);
Bx = Br*(xo/r);
By = Br*(yo/r);
% dt is the adaptive time step a percent of the
% instantaneous gyroperiod
dt = res/((Bmag*q*p*q*nq*Gamma)/(pi*mp));
% find new velocity
V = RKLorentz(dt,[vox; voy; voz],Bx,By,Bz,Ex,Ey,Ez,Alpha);
vnx = V(1);
vny = V(2);
vnz = V(3);
% find new position
xn = vnx*dt + xo;
yn = vny*dt + yo;
zn = vnz*dt + zo;
% pass coordinate values to k by numpart position matrix
endpos(i,1) = xn;
endpos(i,2) = yn;
endpos(i,3) = zn;
% pass new to old before iterating
xo = xn;
yo = yn;
zo = zn;
vox = vnx;
voy = vny;
voz = vnz;

```

```

else
    % pass coordinate values to k by numpart position matrix
    endpos(i,1) = xn;
    endpos(i,2) = yn;
    endpos(i,3) = zn;
end
end

%% Closest approach locator
% extract Point Of Closest Approach (POCA) from data
i=1;
for i=1:k
    % calculate position magnitude
    posmag(i) = ((endpos(i,1)^2)+(endpos(i,2)^2)+...
        (endpos(i,3)^2))^(1/2);
end
% determine minimum position magnitude
posmagmin = min(posmag);
i=1;
for i=1:k
    % fill every other point in the array with zeros to let the
    % find() function find the index
    if (posmag(i) ~= posmagmin)
        posmag(i) = 0;
    end
end
% record the closest approach points in an array of length numpart
clap(h,1) = ((endpos(find(posmag),1)^2)+...
    (endpos(find(posmag),2)^2))^(1/2); % radius
clap(h,2) = endpos(find(posmag),3); % z-position
end

toc%%%%%%%%%%%%%%
%%%%%%%%%%%%%%

```

VITA

Benjamin Alan Klamm was born in Independence, KS on November 10th, 1985. After finishing high school in 2004 he attended Embry-Riddle Aeronautical University in Daytona Beach, FL. In the spring of 2008 he received a Bachelors of Science degree in Aerospace Engineering with minors in computer science and mathematics.

In August of 2008 he began graduate studies in the Mechanical, Aerospace and Biomedical Engineering department at the University of Tennessee Space Institute. From summer 2009 to summer 2010 Ben developed a relativistic particle moving code and ran numerical experiments on a hybrid shield system. He will be graduating with a Master of Science degree in Aerospace Engineering in the summer of 2010. He plans on continuing his doctoral education at the University of Tennessee Space Institute.